Changes in the Extremes of the Climate Simulated by CCC GCM2 under CO$_2$ Doubling

FRANCIS W. ZWIERS* AND VIATCHESLAV V. KHARIN*

Canadian Centre for Climate Modelling and Analysis, University of Victoria, Victoria, British Columbia, Canada

ABSTRACT

Changes due to CO$_2$ doubling in the extremes of the surface climate as simulated by the second-generation circulation model of the Canadian Centre for Climate Modelling and Analysis are studied in two 20-yr equilibrium simulations. Extreme values of screen temperature, precipitation, and near-surface wind in the control climate are compared to those estimated from 17 yr of the NCEP–NCAR reanalysis data and from some Canadian station data.

The extremes of screen temperature are reasonably well reproduced in the control climate. Their changes under CO$_2$ doubling can be connected with other physical changes such as surface albedo changes due to the reduction of snow and sea ice cover as well as a decrease of soil moisture in the warmer world.

The signal in the extremes of daily precipitation and near-surface wind speed due to CO$_2$ doubling is less obvious. The precipitation extremes increase almost everywhere over the globe. The strongest change, over northwest India, is related to the intensification of the summer monsoon in this region in the warmer world. The modest reduction of wind extremes in the Tropics and middle latitudes is consistent with the reduction of the meridional temperature gradient in the 2×CO$_2$ climate. The larger wind extremes occur in the areas where sea ice has retreated.

1. Introduction

While change in the long-term climatic mean state will have many important consequences, the most acute effects of climate change may come about from changes in the intensity and frequency of climatic extremes. For example, the viability of many crops is constrained by the number of frost-free days per year, the frequency and duration of high temperature events that expose crops to damage from heat stress, and the availability of moisture. Insurance schemes spread risk across large pools of users and a number of years by assessing premiums actuarially from historical claims data, historical extreme weather event data, and other related data. Changes in the frequency and/or intensity of extreme events will affect these economic risk sharing arrangements. Human health is affected by weather extremes directly through the physiological effects of heat and cold and indirectly by floods, pollution episodes, and the like.

It is therefore of great interest to document the extremes of surface temperature, the wind, and precipitation that are simulated by a general circulation model (GCM) and to estimate the changes that take place in the simulated climate with a doubling of CO$_2$.

Relatively little work of this sort has been reported with regard to either extreme winds or temperature. Windelband and Sausen (1993) document some aspects of the extreme wind climatology of the Max Planck Institute for Meterology coupled ocean-atmosphere model (ECHAM1/LSG) and the changes that occur under the International Panel on Climate Change (IPCC) scenario A (Houghton et al. 1990). In addition, there have been a variety of studies on the ability of models to simulate the extratropical storm tracks (Lambert 1995; Lambert et al. 1995; König et al. 1993; Hall et al. 1994; Murphy 1995; Carnell et al. 1996; Senior 1995; Bromwich and Tzeng 1994; Beersma et al. 1997) and tropical cyclones (e.g., Bengtsson et al. 1995, 1996). Many authors have examined simulated daily minimum and maximum surface temperature and the changes in diurnal range that occur with increasing CO$_2$ (see, e.g., Mearns et al. 1990; Cao et al. 1992; Rind et al. 1989). Windelband and Sausen (1993) examined some aspects of mini-

---

* Additional affiliation: Department of Mathematics and Statistics, University of Victoria, Victoria, British Columbia, Canada.

Corresponding author address: Dr. Francis W. Zwiers, Canadian Centre for Climate Modelling and Analysis, University of Victoria, P.O. Box 1700, Victoria, BC V8W 2Y2, Canada.
E-mail: Francis.Zwiers@ec.gc.ca

mum and maximum temperature extremes simulated with the ECHAM1/LSG model (Cubasch et al. 1992) in a control simulation and the changes that occur in a transient simulation in which CO_2 concentrations increase as in IPCC scenario A. Several authors [see, e.g., Hennessy and Pittock (1995) and references cited therein] have concerned themselves with imputing changes in surface temperature extremes under climate change from changes in means and variances.

Substantially more work has been reported on the ability of models to simulate drought and precipitation extremes. Mearns (1993) reviews part of this literature. McGuffie et al. (1998, manuscript submitted to *Int. J. Climatol.*) intercompare equilibrium simulations from five models and report that return periods for intense precipitation events tend to be shorter in all models. Several others obtain similar results in equilibrium experiments (see Houghton et al. 1996, chapter 6). Some authors (e.g., Noda and Tokioka 1989; Gordon et al. 1992; Cubasch et al. 1995) have examined the change in the frequency distributions of rainfall events in a warmer climate and show that in the regions considered, intense rainfall events will occur more frequently whereas events of moderate intensity will occur less frequently. In contrast, Parey (1994) does not find evidence for significant change in the return period of heavy rainfall events in the Laboratoire de Meteorologie Dynamique (LMD) model under CO_2 doubling and tripling. Cubasch et al. (1995) also examined the duration of simulated dry spells and showed that dry spells are generally longer in extratropical regions in ECHAM3 under CO_2 doubling and tripling.

In this paper we describe changes in the extremes of the surface climate simulated in an equilibrium doubled CO_2 experiment (Boer et al. 1992) conducted with the second-generation general circulation model (CCC GCM2; McFarlane et al. 1992) of the Canadian Centre for Climate Modelling and Analysis (CCCma). CCC GCM2 is a spectral model with T32 horizontal resolution and 10 levels in the vertical. The model uses a hybrid vertical coordinate system that is terrain following near the surface and coincides with pressure near the top of the atmosphere. The model's "physics" (clouds, convection, radiation, etc.) are computed in physical space on a 96×48 point Gaussian grid (approximately 3.75° lat $\times$ 3.75° long). The model has an interactive lower boundary that consists of a mixed layer ocean model, thermodynamic ice model, and bucket-type soil moisture model in which bucket depth depends upon vegetation type.

The data used in this study come from 20-yr $1\times CO_2$ and $2\times CO_2$ equilibrium simulations. McFarlane et al. (1992) and Boer et al. (1992) describe the first 10 yr of these simulations. Specifically, we analyze simulated daily minimum and maximum screen level (2 m) temperature (denoted T_{min} and T_{max}), 24-h accumulated precipitation P, and instantaneous 1000-mb wind speed S as calculated from velocity vector components at the 1000-mb level sampled twice daily. We use 1000-mb wind speed because instantaneous anemometer height (10 m) wind speed was not available from CCC GCM2.

Comparison of the extreme values of the control climate with those of the observed climate is difficult at best. Although observed variables are point measures, simulated variables represent areas at least the size of a grid box (approximately 3×10^4 km^2 at midlatitudes) and are subject to the effects of a smoothly varying surface topography. They certainly do not include the microclimatological effects that influence station data. Nonetheless, we will attempt some comparisons between simulated and "observed" extremes.

To produce comparable global maps of extreme value statistics we use the National Centers for Environmental Prediction–National Center for Atmospheric Research (NCEP–NCAR) reanalysis data (Kalnay et al. 1996) for 1979–95 inclusive. These data are produced by a state-of-the art analysis/forecast system. The data are available on a 192×94 Gaussian grid that has approximately double the resolution of CCC GCM2. We also make some comparisons with extremes estimated from station data collected in Canada. We use daily records of T_{max} and T_{min} from about 160 stations, and 24-h rainfall extremes derived from about 500 stations (Hogg and Carr 1985). The station temperature records vary in length from 9 to 120 yr with the average length about 50 yr. The precipitation record lengths vary from 10 to 79 yr with the average length 25 yr.

The outline for the remainder of this paper is as follows. The methodology we use is very briefly described in section 2. Changes in the mean state and high-frequency variability that take place under CO_2 doubling are briefly described in section 3. Some characteristics of the extremes of the simulated climate are described in section 4, and changes under CO_2 doubling are described in section 5. A summary and conclusions are presented in section 6.

2. Methodology

Two approaches are used to characterize the extremes of the simulated climate. We estimate 10-, 20-, and 50-yr return values of the simulated climate at every grid point by applying a more or less standard extreme value analysis technique to the annual extremes (the maxima of T_{max}, $-T_{min}$, P, and S), and we compute a number of descriptive statistics such as threshold crossing frequency. The latter will be described as the need arises. The extreme value analysis technique is described here briefly because it departs somewhat from methods that have been used traditionally in atmospheric science and hydrology (see, e.g., Tabony 1983; Revfeim and Hessel

1984; Tiago de Oliveira 1986; Smith 1989; Buishand 1989; Farago and Katz 1990).

Extreme value analysis is performed in this study by fitting the generalized extreme value (GEV) distribution,

$$
F(x) = \begin{cases} \exp\{-[1 - k(x - \xi)/\alpha]^{1/k}\}, & k < 0, \quad x < \xi + \alpha/k, \\ \exp\{-\exp[-(x - \xi)/\alpha]\}, & k = 0, \\ \exp\{-[1 - k(x - \xi)/\alpha]^{1/k}\}, & k > 0, \quad x > \xi + \alpha/k, \end{cases}
$$

to the sample of annual extremes at each grid point using the method of L moments (Hosking 1990, 1992). Here $F(x)$ is the (cumulative) distribution function of the random variable X (annual extreme in our case), which is the probability of observing a realization of X that is smaller than the value x. The distribution has three adjustable parameters ξ, α, and k, which determine its *location, scale,* and *shape,* respectively. Depending on the shape parameter k, the GEV distribution can represent any of the three possible asymptotic extreme value (EV) distributions (i.e., EV-I, EV-II, or EV-III; see, e.g., Gumbel 1958; Leadbetter et al. 1983).

The use of the GEV distribution is justified by the fact that, under fairly general conditions, the distribution of the maximum of a sample of independent and identically distributed variables converges to the GEV distribution, as the length of the sample goes to infinity (Gnedenko 1943). The rate of convergence to the asymptotic distribution is affected by the shape of the upper tail of the distribution of the sampled random

variable. Fast convergence has been reported for the exponentially distributed variables (Leadbetter et al. 1983). For other than exponential distributions, the speed of convergence can be much slower (e.g., Davis 1982). Also, Fisher and Tippett (1928) showed that the convergence is slow for a normal parent distribution.

For $k = 0$ the GEV distribution reduces to the Gumbel, or EV-I distribution, which is of particular interest since it is a limiting distribution of extreme maximal values drawn from a parent distribution, which may be one of several common types, including exponential, normal, and lognormal (e.g., Leadbetter et al. 1983). When $k < 0$ (>0) the GEV distribution has a wider (narrower) tail than the EV-I distribution.

The effect of the parameter k on the shape of the extreme value distribution is demonstrated in Fig. 1. The left panel displays the probability density function $\rho(x) \equiv dF(x)/dx$. The solid curve depicts the EV-I distribution for $\xi = 0$ and $\alpha = 1$. Long- and short-dashed curves represent the EV-II ($k = -0.2$) and EV-III ($k =$
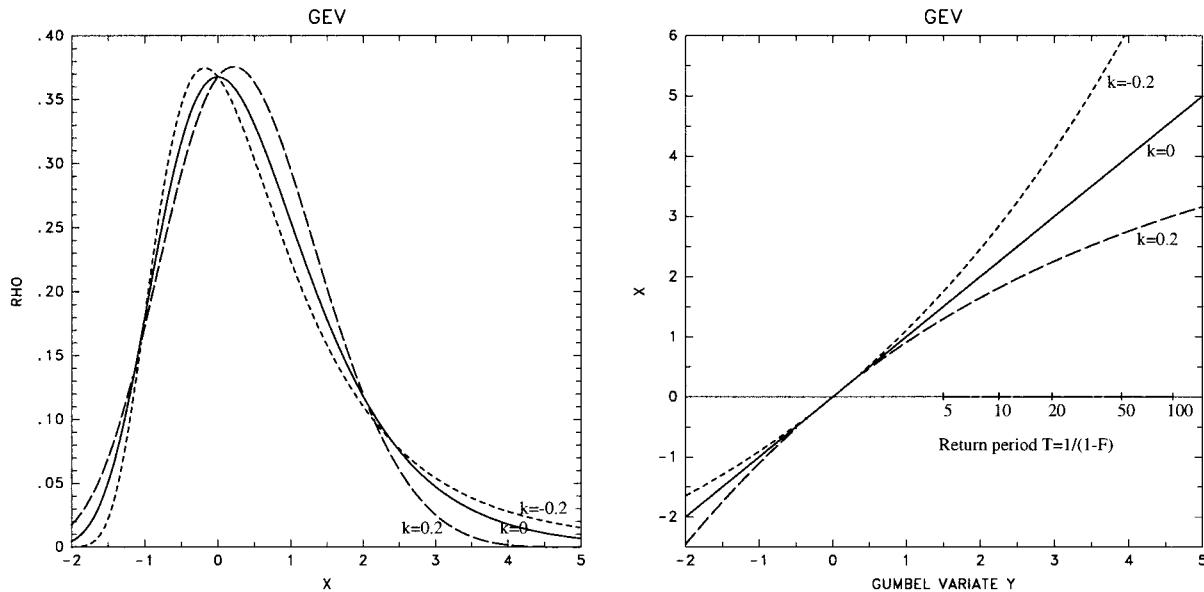

Fig. 1. Probability density function $\rho(x) \equiv dF(x)/dx$ of the GEV distribution plotted against random variable x (left panel) and random variable x plotted against the reduced Gumbel variate $y \equiv -\ln(-\ln F)$ (right panel) for the location parameter $\xi = 0$; scale parameter $\alpha = 0$; and shape parameters $k = 0$ (solid lines), $k = 0.2$ (long-dashed lines), and $k = -0.2$ (short-dashed lines).

0.2) distributions, respectively. In extreme value studies, the (cumulative) distribution function $F(x)$ is often transformed to a new variable $y = -\ln(-\ln F)$, known as the reduced Gumbel variate, so that the EV-I distribution is represented by a straight line (right panel of Fig. 1). The return period, which is the average waiting time between extremes of size x or larger, is also indicated on the horizontal axis of the graph. The return period for a given value of x is given by $T = 1/[1 - F(x)]$. Equivalently, the return value for a given waiting time T is the value of X that is exceeded once every T time units (typically years). The T time unit return value of X is the value of x that satisfies $F(x) = 1 - 1/T$. For negative (positive) k, the return values grow more rapidly (more slowly) than those for the Gumbel distribution as the return period becomes larger.

The extremes of all variables considered here likely lie in the "domain of attraction" of the Gumbel distribution since they likely have distributions with exponential-like upper (lower in the case of $T_{\min}$) tails. However, the asymptotic EV distributions may not fit the observed extremes well for a number of reasons. The annual maxima used in this study are formally drawn from samples of the size 365. However, the members of the sample usually come from a cyclostationary process at best [the mean, variance, and covariance of a cyclostationary process are cyclic with period one year; see, e.g., Huang and North (1996)]. For example, annual maximum temperatures in the extratropical latitudes normally occur in summer. Thus the effective size of the sample can be much smaller than 365. Serial correlation in the data also reduces the effective sample size over which the annual maximum is computed. Therefore, the annual maximum may not have the asymptotic EV-I distribution. The introduction of the third parameter k in the GEV distribution improves the fit to the upper tail when the annual maxima are not EV-I distributed. However, note that its use can increase the uncertainty of parameter and return value estimates when the annual maxima are EV-I distributed.

The method of maximum likelihood parameter estimates is asymptotically optimal but they are not necessarily the best for finite sample sizes. We use the method of L moments because it is computationally simpler than the method of maximum likelihood and because L-moment estimators have better sampling properties than the method of maximum likelihood or the method of conventional moments with finite samples. For example, Hosking et al. (1985) showed that for all values of the shape parameter in the range $-0.5 < k < 0.5$, and for all sample sizes up to 100, estimates obtained by the method of L moments have root-mean-square error that is lower than or comparable to maximum likelihood estimates.

Here L moments are defined in terms of the expected values of *order statistics*. If $\{X_1, X_2, \ldots, X_n\}$ represents a sample of n independent realizations of a random variable X, then the order statistics $\{X_{1:n}, X_{2:n}, \ldots, X_{n:n}\}$

are obtained simply by sorting the sample in ascending order. The subscript $k{:}n$ indicates the kth smallest number in the sample of length n. The first three L moments (Hosking 1990) are defined as

$$\lambda_1 = EX,$$

$$\lambda_2 = \frac{1}{2}E(X_{2:2} - X_{1:2}), \quad \text{and}$$

$$\lambda_3 = \frac{1}{3}E(X_{3:3} - 2X_{2:3} + X_{1:3}),$$

where E denotes expectation. When X has the GEV distribution, they are given by

$$\lambda_1 = \xi + \alpha[1 - \Gamma(1 + k)]/k,$$

$$\lambda_2 = \alpha(1 - 2^{-k})\Gamma(1 + k)/k, \quad \text{and}$$

$$\lambda_3 = \lambda_2[2(1 - 3^{-k})/(1 - 2^{-k})].$$

If we now let $\{X_1, X_2, \ldots, X_n\}$ represent a sample of n annual maxima, then the corresponding unbiased estimators of $\lambda_1, \ldots, \lambda_3$ are

$$l_1 = \sum_i X_i/n,$$

$$l_2 = \frac{1}{2}\sum_{i>j}(X_{i:n} - X_{j:n})/C_2^n, \quad \text{and}$$

$$l_3 = \frac{1}{3}\sum_{i>j>k}(X_{i:n} - 2X_{j:n} + X_{k:n})/C_3^n,$$

where $C_k^n = n!/[k!(n-k)!]$. Since the sample L moments are simple linear combinations of the sample of annual maxima, they have much better sampling properties than the conventional sample moments and can more accurately discriminate between competing distributional models for a sample of extremes (Hosking 1992).

The method of L moments fits the GEV distribution by choosing parameters ξ, α, and k so that the first three population L moments, λ_1, λ_2, and λ_3, match the corresponding estimates. The resulting method of L moment estimators are given by

$$\hat{k} = 7.8590z + 2.9554z^2,$$

$$\hat{\alpha} = l_2\hat{k}/[1 - 2^{-\hat{k}}\Gamma(1 + \hat{k})], \quad \text{and}$$

$$\hat{\xi} = l_1 + \hat{\alpha}[\Gamma(1 + \hat{k}) - 1]/\hat{k},$$

where $z = 2/(3 + l_3/l_2) - \ln 2/\ln 3$.

Having fitted the GEV distribution to a sample of annual maxima, the T-year return value is estimated by inverting the fitted distribution function $\hat{F}(x) = 1 - 1/T$ to obtain

$$\hat{X}_{RV_T} = \hat{\xi} + \hat{\alpha}\{1 - [-\ln(1 - 1/T)]^{-\hat{k}}\}/\hat{k}. \tag{1}$$

The uncertainty of this estimate is difficult to obtain analytically. A practical approach is to estimate the sampling uncertainty using a variant of the bootstrap (Efron 1982). The parametric bootstrap is used in this paper.

TABLE 1. Globally averaged annual mean, daily standard deviation, and 10-, 20-, 50-yr return values (RV) of T_{max} (°C), T_{min} (°C), P (mm day^{-1}), and S (m s^{-1}) in the control (1 × CO_2) climate and their change simulated under CO_2 doubling (Δ).

	T_{max} (°C)		T_{min} (°C)		P (mm day^{-1})		S (m s^{-1})	
	1 × CO_2	Δ	1 × CO_2	Δ	1 × CO_2	Δ	1 × CO_2	Δ
Mean	15.48	3.37	11.69	3.67	2.75	0.11	8.70	−0.23
Std dev	1.54	−0.18	1.84	−0.27	6.72	0.49	3.59	−0.08
10-yr RV	24.21	3.14	−0.85	5.00	72.97	7.78	23.66	0.59
20-yr RV	24.51	3.14	−1.49	5.06	81.25	9.03	24.59	0.58
50-yr RV	24.86	3.12	−2.30	5.16	92.03	10.77	25.78	0.64

In this procedure the samples of size n are generated from the fitted GEV distribution repeatedly. A return value is estimated from each generated sample by fitting and inverting a GEV distribution as derived above. The 5th and 95th percentiles of the resulting collection of return value estimates are then used as lower and upper 90% confidence bounds for the true T-year return value.

3. CO_2-induced changes in the mean state and variability of the simulated climate

McFarlane et al. (1992) describes CCC GCM2 and the 1×CO_2 climate that it simulates. Boer et al. (1992) describes the changes that occur under CO_2 doubling. We briefly review and augment some of these results here for the variables considered in this paper. Global averages and some other summary statistics are given in Table 1.

a. Daily minimum and maximum temperature

Figure 2 displays the change under CO_2 doubling of T_{min} for December–February and June–August. We see that there are modest changes of 2°–4°C over the oceans and tropical landmasses, larger changes of 4°–12°C over extratropical landmasses, and very large changes of 12°–20°C in high-latitude regions where the sea ice has retreated and the atmosphere comes into direct contact with the ocean. The spatial pattern of the signal in daily minimum screen temperature T_{min} is similar to that of the change in daily mean screen temperature shown in Boer et al. (1992) for the first 10 yr of the model simulations. However, the amplitude of the change of T_{min} in middle latitudes over the continents and in high latitudes is up to 4°C higher than that for the mean screen temperature.

The change in T_{max} (not shown) is similar, but the amplification resulting from the change in albedo feedback at high latitudes is not as pronounced. The amplitude is generally smaller over the continents than that for T_{min} although there is an increase of 8°–10°C in the center of the Eurasian continent in summer. This increase is related to the decrease of soil moisture in the corresponding area and thus to the reduced soil heat capacity allowing stronger diurnal variations of screen temperature. Globally averaged, the annual changes in

T_{min} and T_{max} are 3.67°C and 3.37°C, respectively (Table 1).

Accompanying the increase in mean temperature is an overall reduction in daily screen temperature variability in most parts of the world (Table 1). The annual cycle, defined as the first four harmonics, is subtracted from each year before calculating the standard deviation. The global mean of the T_{min} daily standard deviation decreases from 1.84°C in the simulated 1×CO_2 climate to 1.57°C in the 2×CO_2 climate. As with the mean, the change in daily T_{max} variability is not as great as it is for T_{min}. The globally averaged daily T_{max} standard deviation decreases from 1.54°C to 1.36°C.

b. Precipitation

Figure 3 displays changes in the annual mean daily precipitation rate that occur in the climate of CCC GCM2 with CO_2 doubling. There is a general increase of precipitation in high latitudes and marginal drying in midlatitudes. Shifts in the distribution of precipitation over the Maritime Continent, southern Asia, and the Indian Ocean are connected with a strengthening of the Asian summer monsoon in the warmer climate. The daily variability of the simulated precipitation (Table 1) increases marginally.

The changes in the annual precipitation rate shown in Fig. 3 are in general agreement with the precipitation signal found by Boer et al. (1992) in the first 10 yr. The globally averaged annual mean precipitation rate increases from 2.75 mm day^{-1} in the 1×CO_2 climate to 2.86 mm day^{-1}. The "hydrological sensitivity" of CCC GCM2 is generally weaker than that of other models (Boer 1993) as a consequence of cloud albedo feedback. The global average of the daily standard deviation increases from 6.72 mm day^{-1} to 7.22 mm day^{-1}.

c. Wind speed

The change in the annual mean 1000-mb wind speed as simulated by CCC GCM2 under CO_2 doubling is shown in Fig. 4. Boer (1995) shows that, consistent with the reduced pole-to-equator temperature gradient, the baroclinic part of the energy cycle in the atmosphere decreases, the eddies weaken, and the overall rate at which the system works decreases in the warmer world.
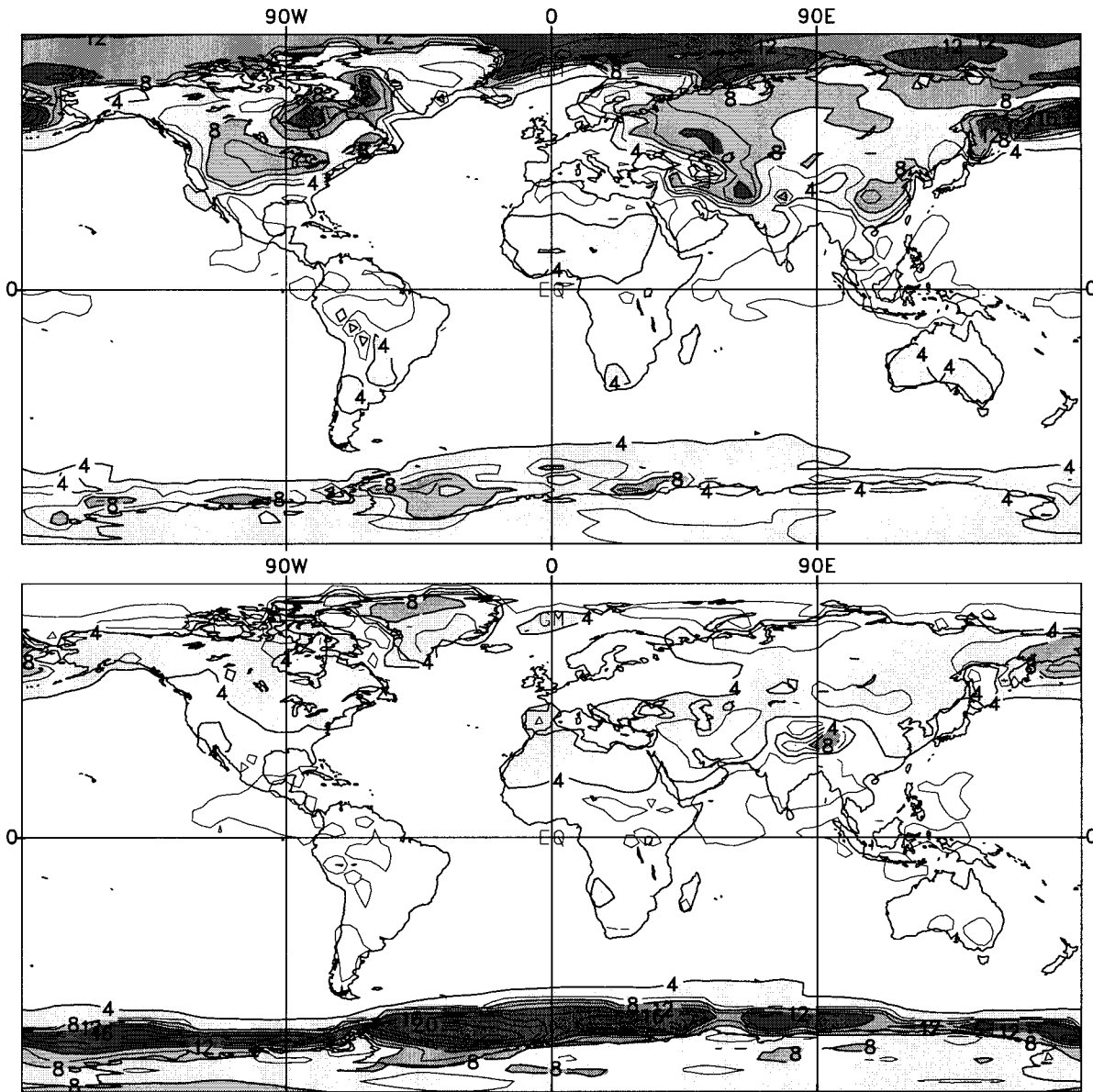
FIG. 2. Change in daily minimum screen temperature for December–February upper panel) and for June–August (lower panel) simulated by CCC GCM2. Contour interval: 2°C. Light, medium, and dark shading indicates changes greater than 4°, 8°, and 12°C, respectively.

Correspondingly, near-surface wind speeds decrease marginally everywhere except at very high latitudes. The globally averaged annual mean wind speed decreases from 8.70 m s^{-1} to 8.47 m s^{-1}. The largest decreases, which are of the order of 0.7 m s^{-1}, occur in the roaring 40's of the Southern Hemisphere, in the subtropical northern Pacific, and in the Northern Hemisphere storm tracks. The reduction of wind speed in these areas is in rough agreement with the patterns of the mean sea level pressure change described by Boer et al. (1992). For example, the decrease of wind speed in the zonal belt at about 45°S is accompanied by positive sea level pressure anomalies southward of that latitude in the warmer world. The increase of wind speed

in high latitudes in the $2\times CO_2$ climate is apparently related to reductions in surface roughness that occur where the sea ice retreats. Small decreases in daily standard deviation (from 3.59 m s^{-1} to 3.51 m s^{-1} globally averaged) occur over most of the globe except at very high latitudes.

4. The extremes of the control climate

In this section we document some features of the extremes in the control climate simulated by CCC GCM2. Validation of this aspect of the simulated climate is difficult on a global scale because reliable, observed gridded data comparable to that produced by the model
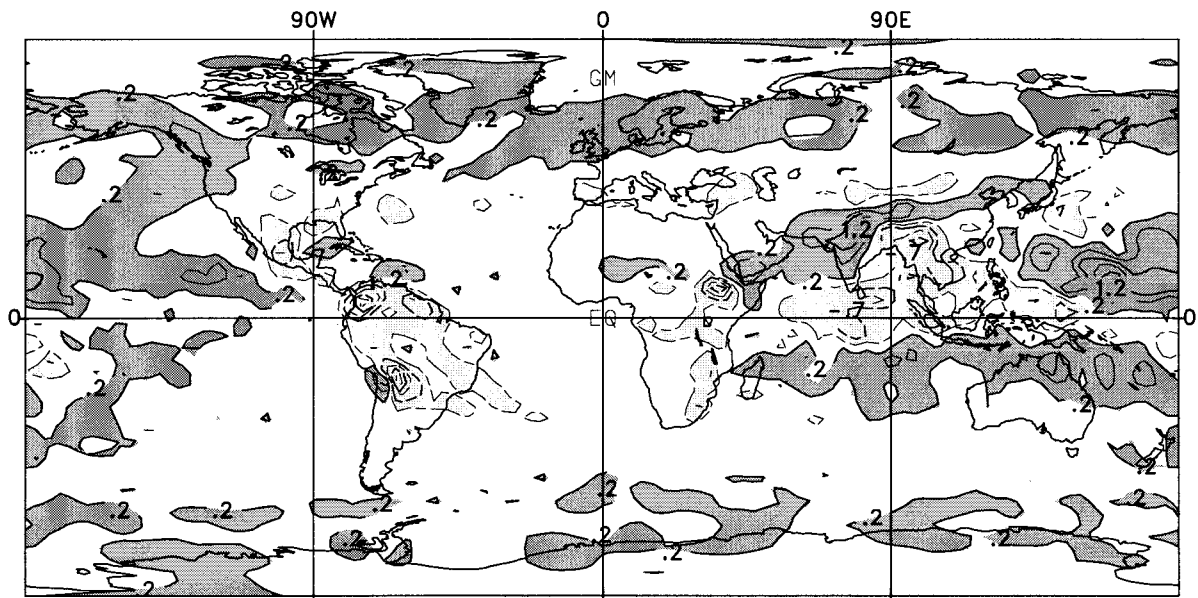
FIG. 3. Change in the annual mean daily precipitation simulated by CCC GCM2. Contour interval: 0.5 mm day^{-1}. Dark (light) shading indicates regions in which the precipitation rate has increased (decreased) by at least 0.25 mm day^{-1}.

is scarce. Our comparisons with ''observations'' on the globe are therefore limited primarily to the NCEP–NCAR reanalysis data. The latter dataset, however, as we will point out in the following discussion, is far from perfect, at least for our purpose. In addition, we use data records of T_{max} and T_{min} from about 160 stations in Canada as well as rainfall data for about 500 Canadian stations (Hogg and Carr 1985) to estimate return values of T_{max}, T_{min}, and P over Canada. Zwiers and Ross (1991) also describe analyses of observed 24-h precipitation extremes at some isolated locations in Canada. In the following we will concentrate mainly on 20-yr return values. The results for 10-yr and 50-yr return values are essentially the same.

a. Screen temperature

Twenty-year return values for daily maximum temperatures (designated $T_{max,20}$) in the simulated $1 \times CO_2$ climate, estimated as described in section 2, are displayed in Fig. 5 (upper panel). Return values over open water are strongly constrained because most incoming solar radiation is either absorbed by the mixed layer ocean or converted into latent heat. Over land there is substantial variability in the conversion of incoming solar radiation into sensible and latent heat in both space and time, and thus much larger extremes (relative to the mean state) can be generated. Very high 20-yr return values ($>45°C$) are found over parts of the western United States (US), the midwestern United States, Argentina, the Sahara, the Iberian peninsula, the Asian deserts, and Australia with isolated regions (the midwestern United States, the Persian Gulf, and the Great Indian Desert) in which there

are return values in excess of 50°C. Global averages in the model are given in Table 1.

The T_{max} return values estimated from the NCEP–NCAR data (not shown) are unrealistically large over the continents due to a known problem in the boundary layer formulation. The reanalysis produced unreliable T_{max} values when near-surface winds were weak (NCEP–NCAR 1997a).

Twenty-year T_{max} return values estimated from the Canadian station data are shown in the lower panel of Fig. 5. These values are generally higher than for the model. For example, the values of $T_{max,20}$ at many stations near the southern border in western and central Canada are in excess of 38°–40°C whereas the corresponding model values are 30°–35°C. Similarly, in other regions of Canada the model underestimates 20-yr return values of T_{max} by about 5°C compared to the observed station data. This can be attributed in part to the fact that the model has a cold bias over North America compared to the observations, which is comparable to the error in the T_{max} return values.

Twenty-year return values of T_{min} (designated $T_{min,20}$) are very similar in the model (Fig. 6, upper panel) and reanalysis data (not shown) on the global scale. The reanalysis T_{min} data is not affected by the boundary layer problem that affects T_{max}, but they may still be unreliable because NCEP inadvertently used the 1973 snow cover for the period 1974–94. Preliminary analysis (E. Kalnay 1997, personal communication) suggests that this error affects 2-m temperature but that the impact is not dominant since its anomalies are driven more by the upper circulation than by the snow cover.
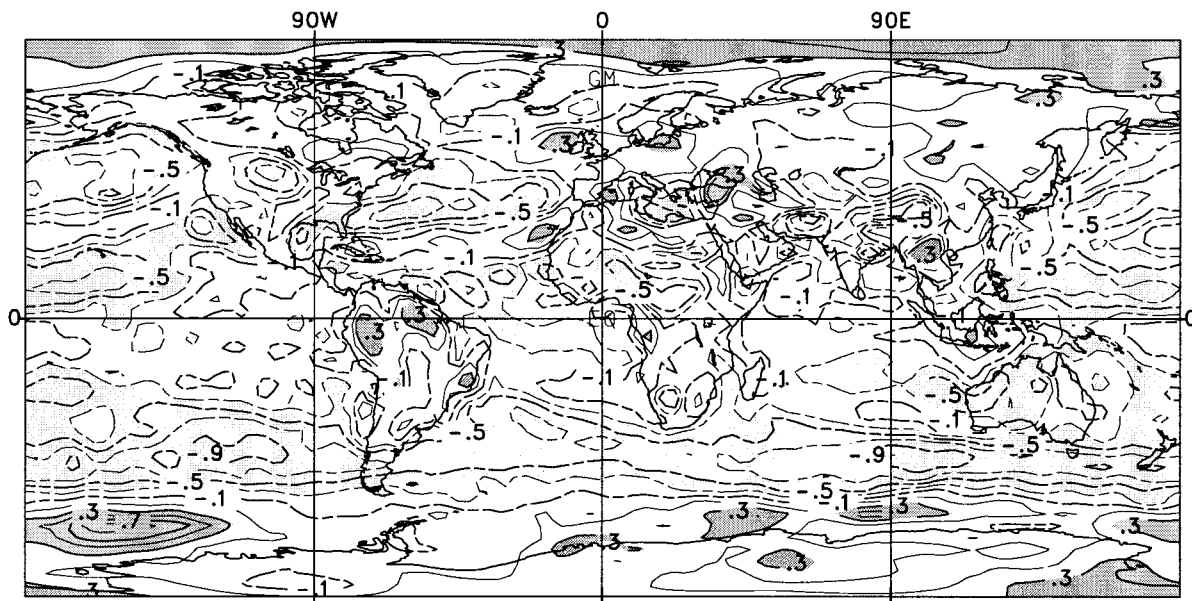
Return values in the model over polar and Northern

FIG. 4. Change in the annual mean 1000-mb wind speed simulated by CCC GCM2. Contour interval: 0.2 m s^{-1}. Dark (light) shading indicates regions in which the wind speed has increased (decreased) by at least 0.3 m s^{-1}.

Hemisphere landmasses appear to be reasonable, whereas those over western Europe are somewhat overestimated. The model also reproduced return values estimated from Canadian station data reasonably well (Fig. 6, lower panel). For example, estimated return values in the lower Great Lakes region range from $-30°C$ to $-35°C$ and return values across the southern Canadian prairies range between $-40°C$ and $-45°C$. Model-derived estimates of $T_{min,20}$ over northern Canada are $5°$–$8°C$ too low.

b. Precipitation

Estimated 20-yr return values of daily precipitation in the control climate and as estimated from station data over Canada are displayed in Fig. 7. The corresponding return value estimates for the NCEP–NCAR data are not shown. The NCEP–NCAR precipitation data does not appear to reproduce daily variability well. Twenty-year return values estimated from NCEP–NCAR data are less than 50 mm day^{-1} over most of the globe, including the tropical regions. Return values greater than 50 mm day^{-1} are seen only in the storm track areas. Thus, the return values seem to be underestimated, drastically so in the Tropics. As an indication, and without any pretension on generality for the whole region, the 20-yr return value of daily precipitation estimated from a 17-yr record at Singapore (1.4°N, 103.9°E) is 207 mm day^{-1}.

The interpretation of GCM-simulated precipitation is an open problem that is beyond the scope of the present paper. Some authors (e.g., Osborn and Hulme 1997) treat simulated precipitation as grid box averages; others (e.g., Skelly and Henderson-Sellers 1996) argue that it

should be treated as gridpoint values. However, regardless of interpretation, the intramonthly and intraseasonal variability in the Tropics seems to be poorly represented in the NCEP–NCAR model forecasts (see also NCEP–NCAR 1997b).

Return values in the Tropics and subtropics in the model reflect the large-scale divergent tropical circulations of the simulated climate. The locations of the upward (high return values) and downward (low return value) branches of these circulations are easily discerned. The very large simulated return values (in excess of 200 mm day^{-1}) in the western tropical Pacific are likely overestimated since CCC GCM2 simulates more precipitation in the Asian summer monsoon outflow area than is observed (McFarlane et al. 1992).

Estimated return values derived from Canadian station data show that, on large spatial scales, the model simulates plausible values over much of Canada. Return values over Atlantic Canada appear to be underestimated by the model. Also, small-scale features such as precipitation over Vancouver Island and southwest of Canada, which depend critically on the interaction between the atmospheric flow and the local topography, are not well reproduced.

c. Wind speed

Comparisons of simulated and observed extreme wind statistics are very difficult for a number of reasons. Local topographic and microclimatological effects cause short time and space scale turbulence that is captured by some types of observations such as the hourly, 1-min mean observations routinely collected by many weather services at anemometer (10 m) height. Clearly
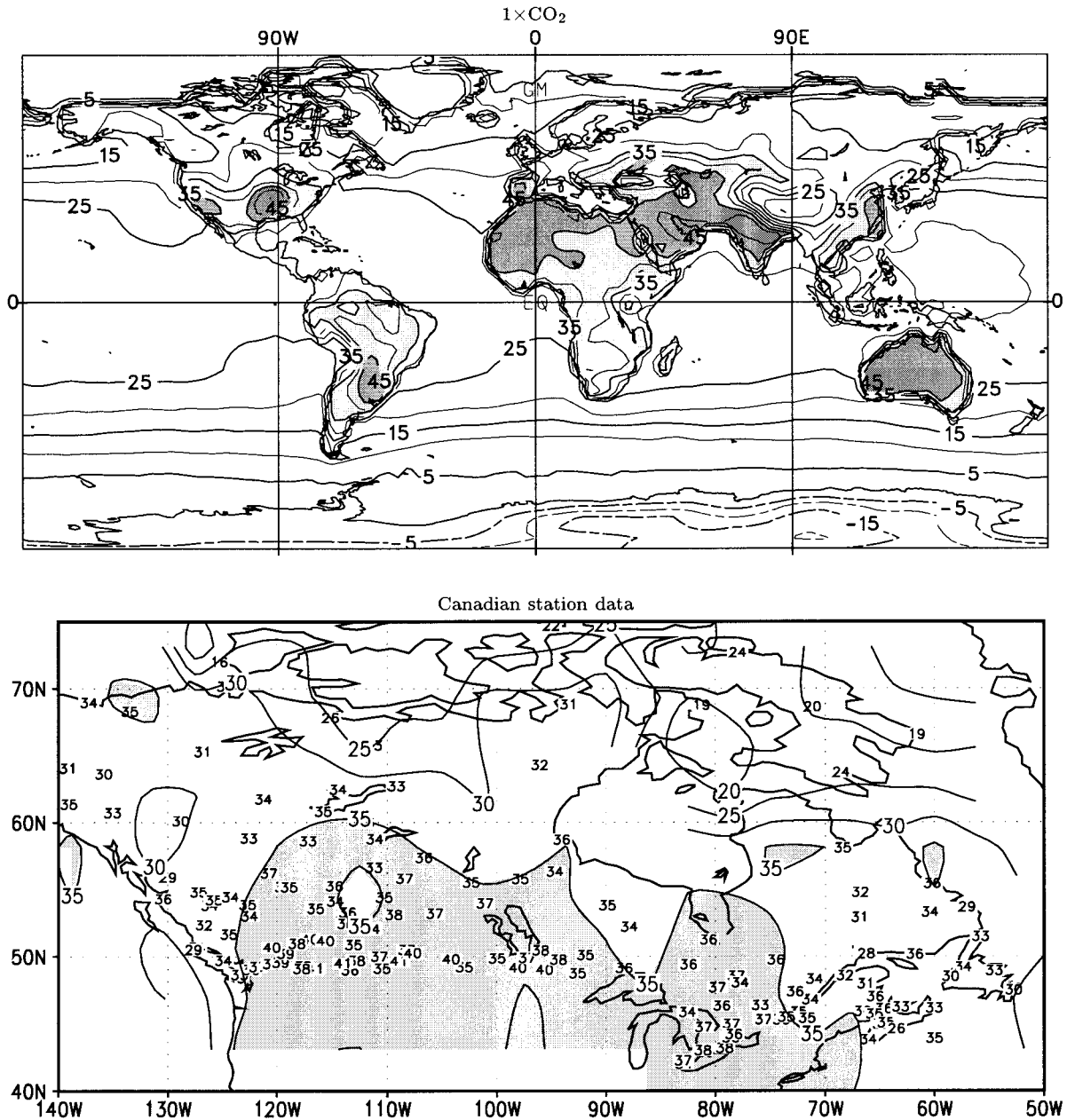
FIG. 5. Twenty-year return values for daily maximum screen temperature simulated by CCC GCM2 (upper panel) and for the Canadian station data (lower panel). Contour interval: 5°C. Light (dark) shading indicates regions in which the 20-yr return values of T_{max} are larger than 35° (45°)C. Numbers in the lower panel display the 20-yr return values for individual stations.

GCMs (even high-resolution forecast models) with their relatively coarse spatial resolutions and time stepping schemes (20 min in the case of CCC GCM2) will not be able to reproduce all aspects of the observed surface wind variability. Also, different sampling schemes are utilized in the model and the observed climate. The simulated annual maxima are obtained from "instantaneous" wind speeds that are sampled once every 12 h (36 model time steps), whereas observed annual maxima are typically computed from 1-min mean wind speeds that are sampled hourly.

Since the instantaneous values of anemometer height wind speed were not available for CCC GCM2, we use 1000-mb wind speed. For this reason we limit the comparison of near-surface wind speed extremes in the model to those in the NCEP–NCAR reanalysis data only. The wind speeds may be unreliable in high elevation areas where the 1000-mb level is below the surface.
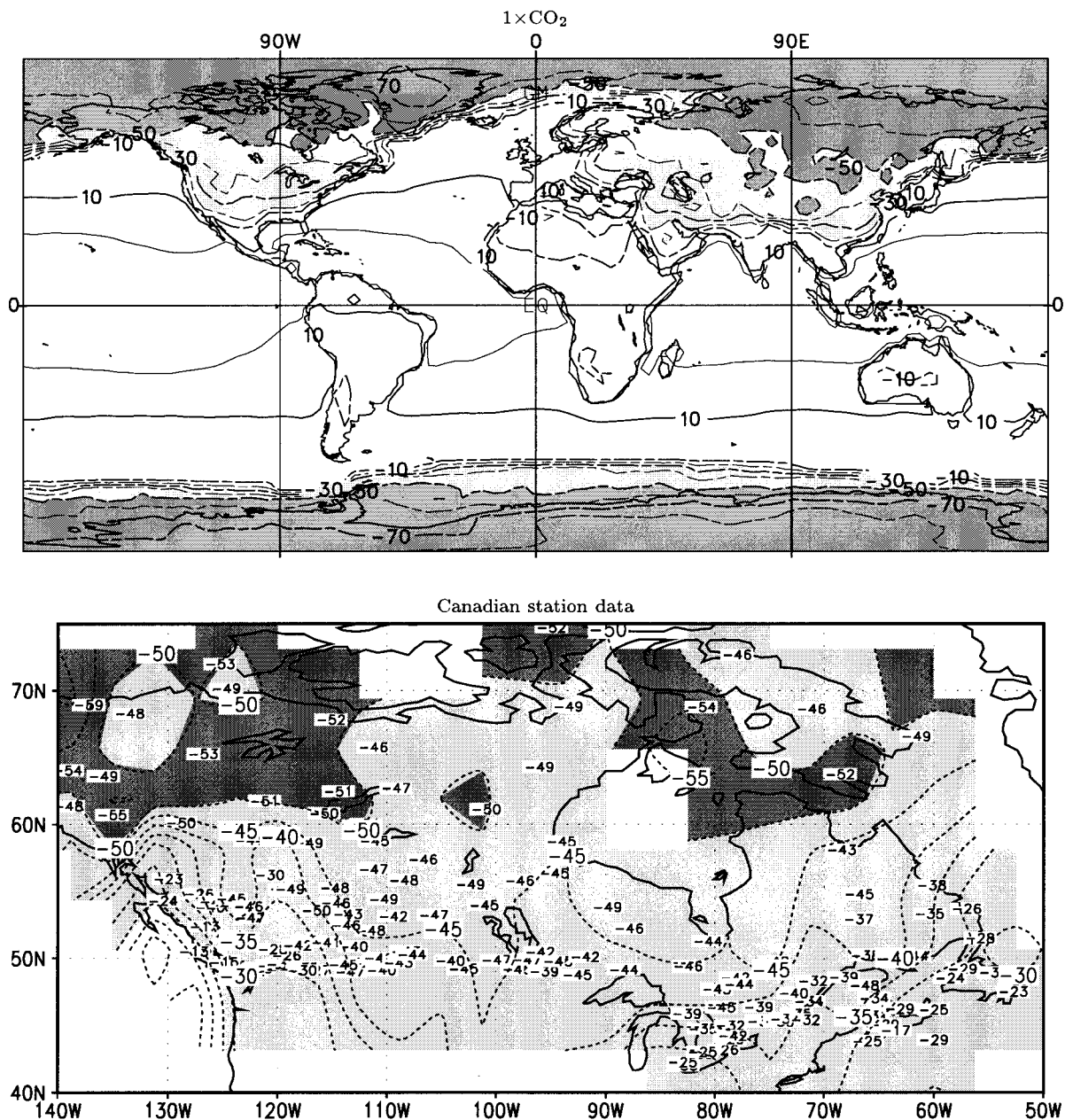
FIG. 6. Twenty-year return values for daily minimum screen temperature simulated by CCC GCM2 (upper panel) and for the Canadian station data (lower panel). Contour interval: 10°C. Light (dark) shading indicates regions in which the 20-yr return values of T_{min} are smaller than $-20°$ $(-50°)$C.

Also, in view of the problems with screen temperature and precipitation, the NCEP–NCAR 1000-mb wind speed data should be considered with care. To reduce data volume, we considered only daily maximum wind speed—that is, the maximum of two instantaneous values per day, hereafter simply called the wind speed. Although the NCEP–NCAR reanalysis data are sampled every 6 h (four values per day), we ignored every second record to obtain comparable statistics.

Before discussing the results of the extreme value

analysis, it should be noted that the mean near-surface wind speed in the model is generally stronger than that in the NCEP–NCAR data; the annual mean 1000-mb wind speed (not shown) in the Northern Hemisphere storm tracks and in the southern roaring 40's are up to 2 m s^{-1} greater. The globally averaged annual mean wind speeds in the model and NCEP–NCAR data are 8.70 and 6.88 m s^{-1}, respectively. McFarlane et al. (1992) also found that the zonal winds simulated by CCC GCM2 in the lower troposphere are stronger than
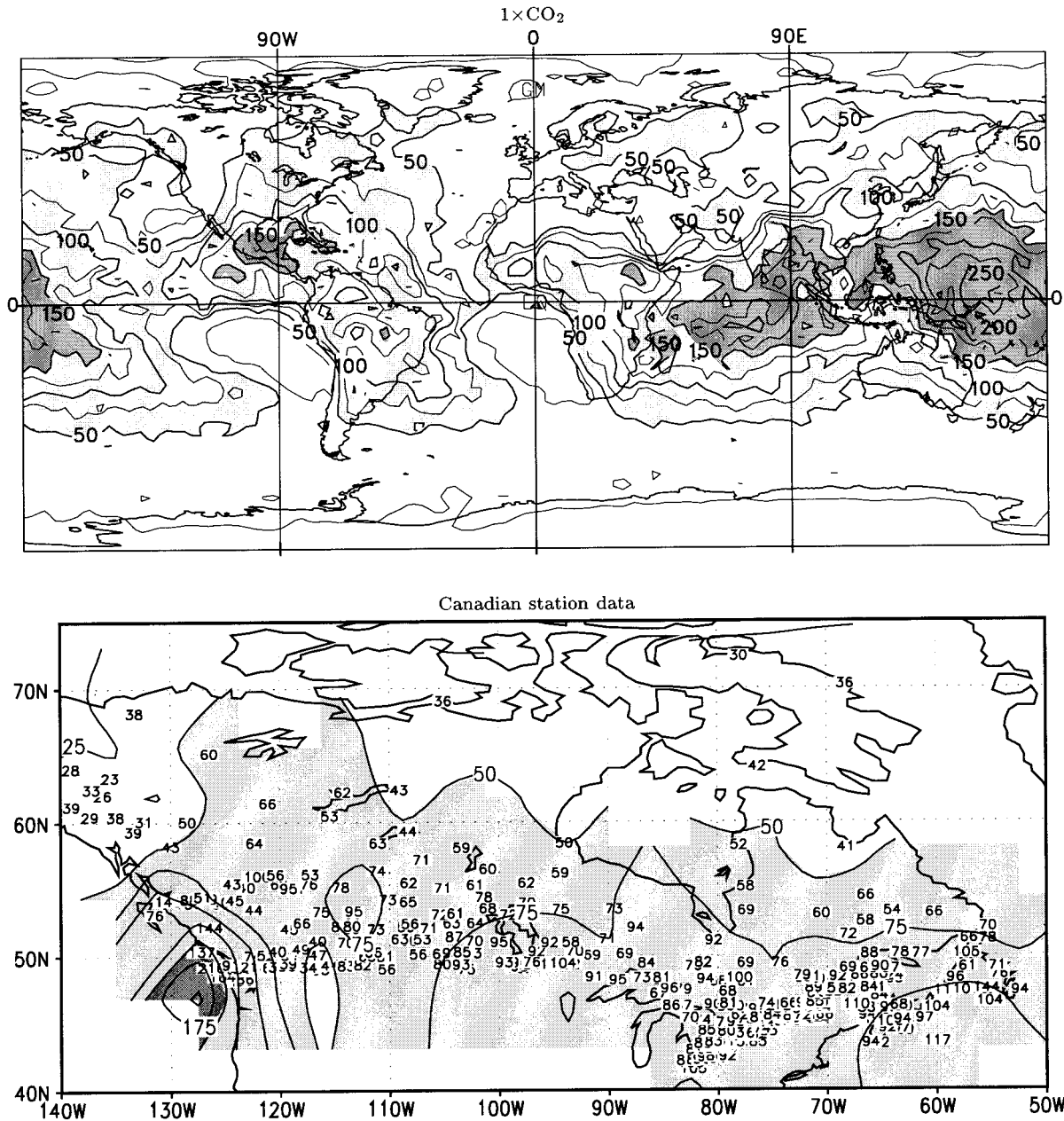
FIG. 7. Twenty-year return values for daily accumulated precipitation simulated by CCC GCM2 (upper panel) and for the Canadian station data (lower panel). Contour interval: 25 mm day^{-1}. Light (dark) shading indicates regions in which the 20-yr return values of daily precipitation are larger than 50 (150) mm day^{-1}. Numbers in the lower panel display the 20-yr return values for individual stations.

those analyzed operationally by NCEP (McFarlane et al. (1992), their Fig. 9).

Twenty-year return value estimates for 1000-mb wind speed are displayed in Fig. 8. The midlatitude storm tracks over the North Pacific and Atlantic Oceans and over the southern circumpolar ocean are clearly apparent. Although comparable return values of 35 m s^{-1} are obtained from both datasets in the North Atlantic region, the model produces extreme winds that are up to 5 m s^{-1} stronger in the North Pacific and in the southern roaring 40's than the

NCEP–NCAR reanalysis. The globally averaged mean 20-yr return value of wind speed is 24.6 m s^{-1} in the model and 19.2 m s^{-1} in the reanalysis data.

Another technique for studying extreme events is to count the number of days per year in which the variable exceeds a certain threshold value. Figure 9 displays the number of "strong wind" days per year in the $1 \times CO_2$ climate and in the NCEP–NCAR reanalysis data. A strong wind day is defined as a day with 1000-mb wind speed greater than 18 m s^{-1} for the model. Considering
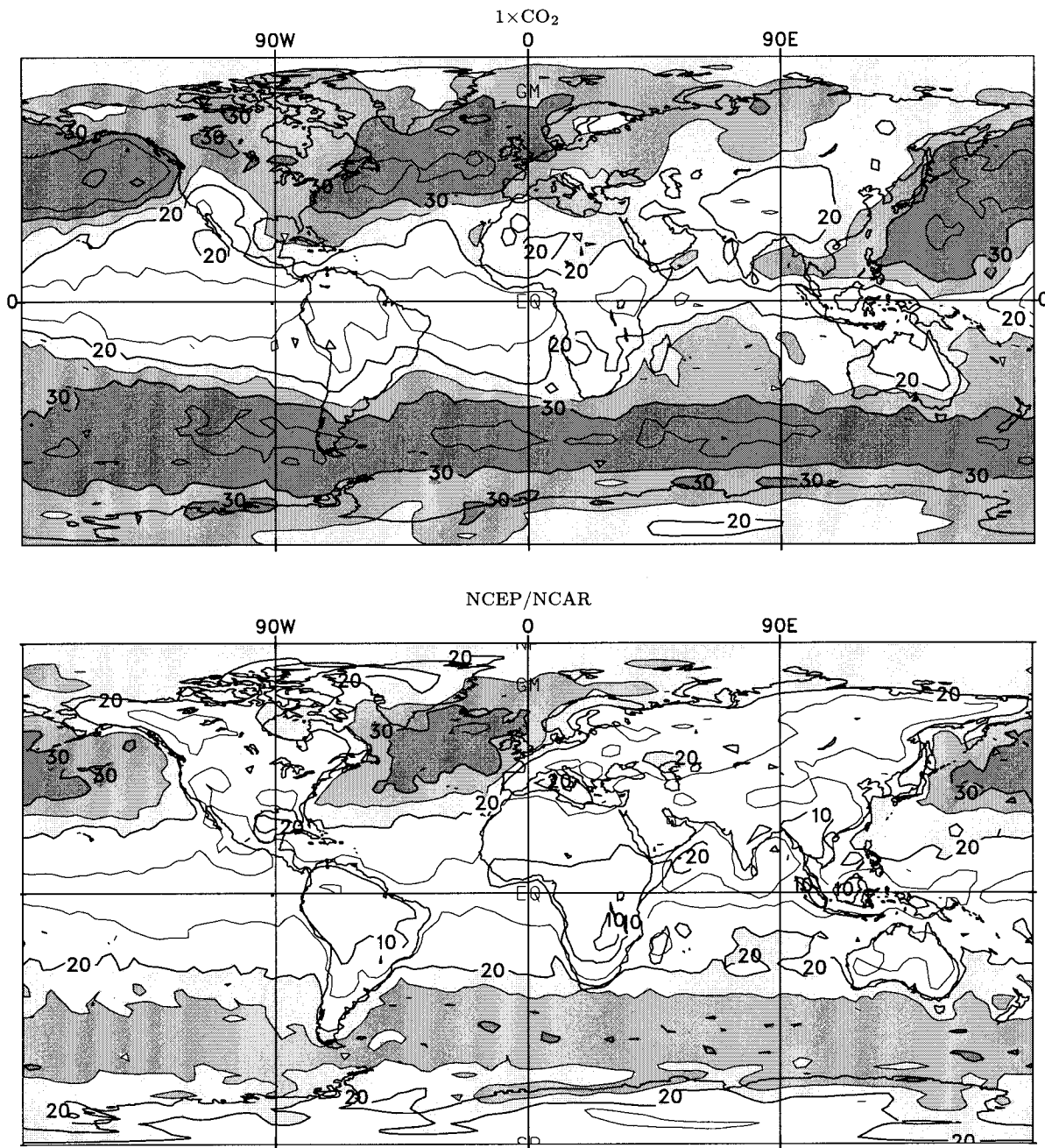
FIG. 8. Twenty-year return values for 1000-mb wind speed simulated by CCC GCM2 (upper panel) and for the NCEP–NCAR data (lower panel). Contour interval: 5 m s^{-1}. Light, medium, and dark shading indicates regions in which the 20-yr return values of wind speed are larger than 20, 25, and 30 m s^{-1}, respectively.

that the surface winds in the model are about 2 m s^{-1} stronger than in the reanalysis data, we decreased the threshold for the NCEP–NCAR data, rather arbitrarily, to 16 m s^{-1} to obtain comparable frequencies of strong wind days. The spatial structure of the resulting strong wind day frequencies is relatively well captured by the model. However there are some differences between the model and reanalysis data that are worth mentioning. In

the model, the strong wind day frequency in the North Pacific storm track is greater than that in the North Atlantic, whereas the opposite is true for the reanalysis data. The local frequency maximum in the northern subtropical west Pacific is stronger in the model than in the reanalysis data. And finally, the model has a more zonal strong wind day frequency distribution in the Southern Hemisphere than the reanalysis.
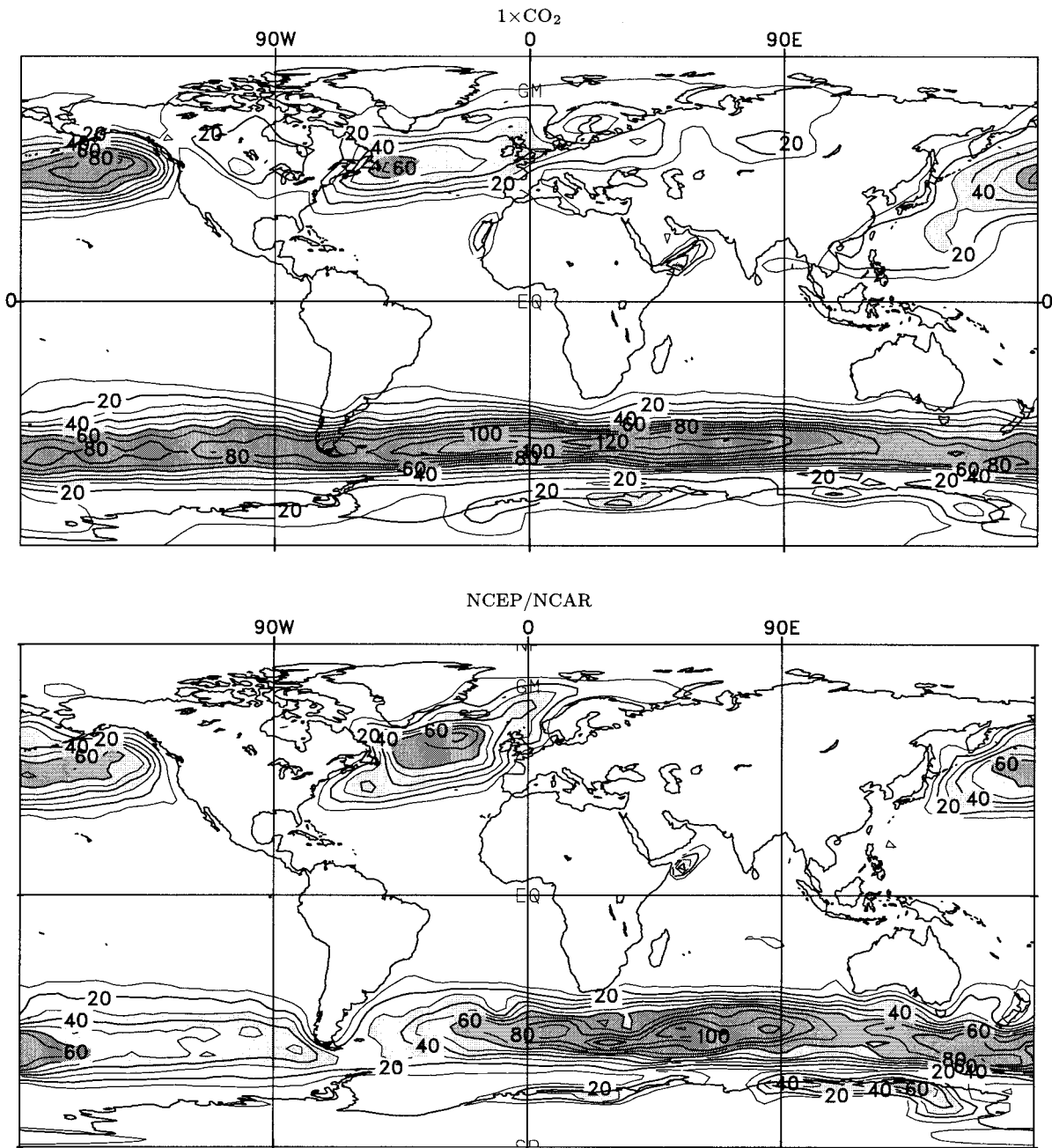
FIG. 9. The number of "strong wind" days per year in the $1 \times CO_2$ climate (upper panel) and in the NCEP–NCAR reanalysis data (lower panel). A "strong wind" day is defined as a day with 1000-mb wind speed greater than 18 m s^{-1} in the $1 \times CO_2$ climate and greater than 16 m s^{-1} in the NCEP–NCAR data. Light (dark) shading indicate regions in which the frequency is larger 30 (60) days yr^{-1}.

An advantage of the threshold crossing technique is that we can identify the time of year in which extremes are more likely to occur. Assuming that the frequency distribution of extremes over the annual cycle has a single maximum, we proceed as follows. First the frequency distribution of strong events over the annual cycle was estimated by classifying the strong wind events according to the day of year on which they occur.

Then we searched for the most compact interval that contains at least 50% of the total number of strong events. The median of these dates is taken as an estimate of the time of year when strong events are mostly likely to occur, and the interval width, or length of the strong wind season, is an indication of whether strong events occur only in a specific season or are distributed more uniformly over the whole year.
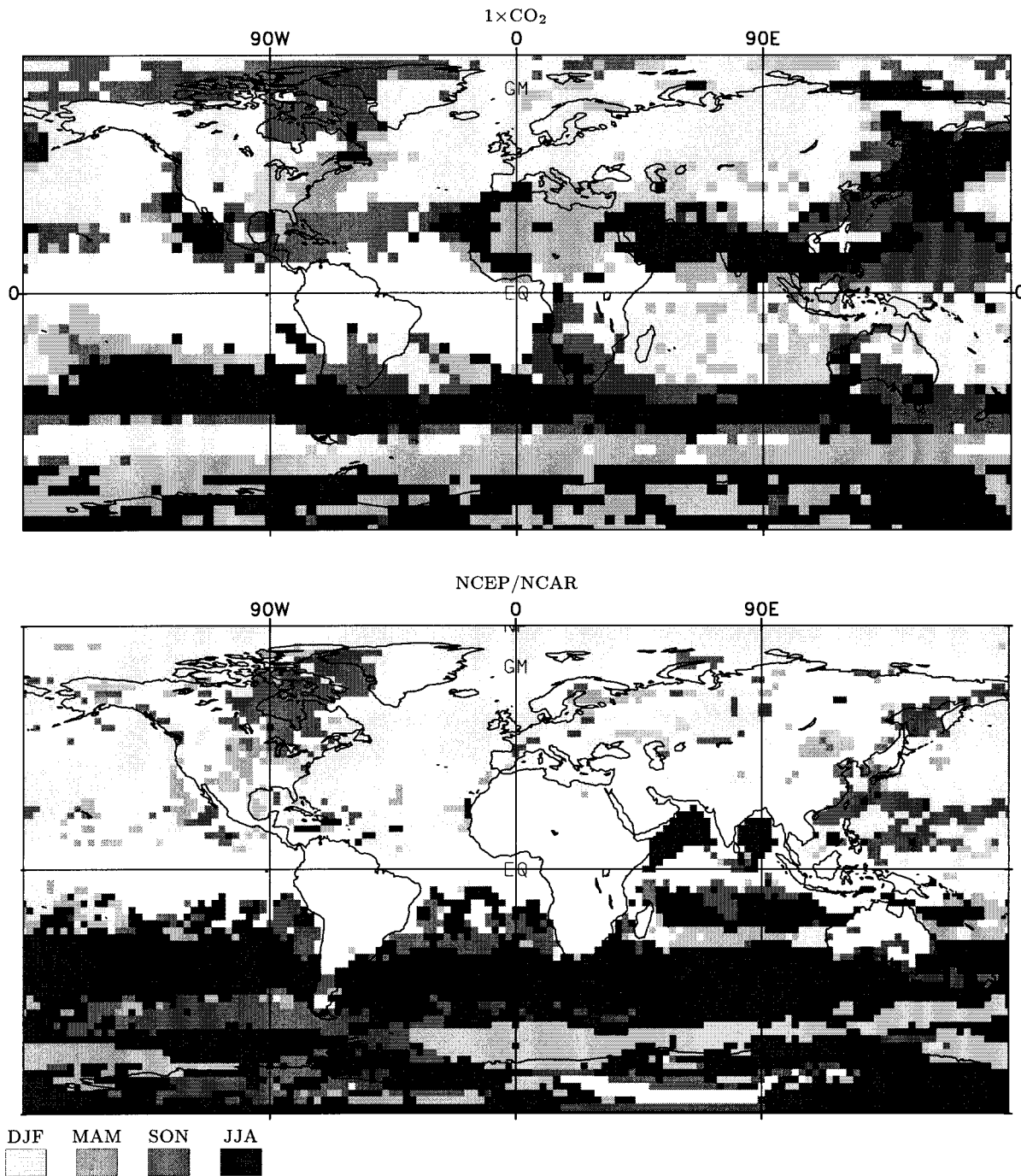
FIG. 10. The season of the median of the most compact interval that contains at least 50% of the total number of strong wind days per year as simulated by CCC GCM2 (upper panel) and for the NCEP–NCAR data (lower panel). A strong wind day is defined as in Fig. 9. Light, middle, heavy, and black shading indicate regions in which the median belongs to the Dec–Feb, Mar–May, Sep–Nov, or Jun–Aug season, respectively.

Figure 10 displays the season in which strong events are mostly likely to occur, calculated as described above, for the control climate and for the reanalysis data. White areas indicate areas with no events exceeding the threshold value. In the NCEP–NCAR reanalysis, light shading dominates in the Northern Hemisphere and dark shading dominates in the Southern Hemisphere indicating that the strong winds predominately occur in winter. The seasonal contrast is not as apparent in the model. Disagreement occurs primarily in areas where the strong
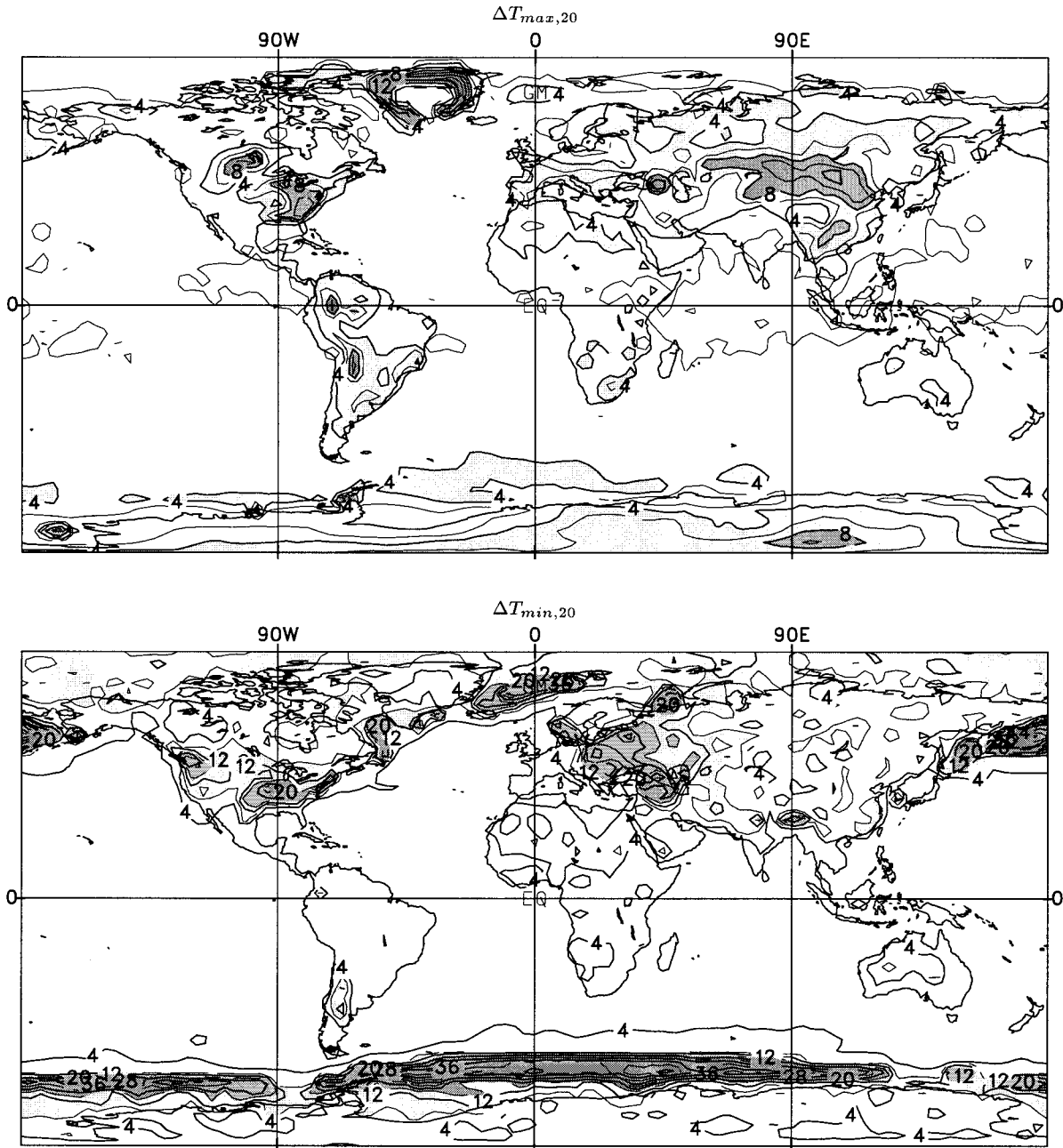
$\Delta T_{max,20}$

$\Delta T_{min,20}$

FIG. 11. The estimated change in 20-yr return values for daily maximum (upper panel) and minimum (lower panel) screen temperature simulated by CCC GCM2 under CO_2 doubling. Contour interval: 2°C for $T_{max,20}$ and 4°C for $T_{min,20}$. Light (dark) shading indicates regions in which the 20-yr return value has increased by at least 4° (8°)C for $T_{max,20}$ and by at least 8° (16°)C for $T_{min,20}$.

wind season is long, and hence, where the median date for strong wind events is poorly estimated.

5. Changes in simulated extremes under CO_2 doubling

a. Screen temperature

The change between the simulated $1 \times CO_2$ and $2 \times CO_2$ climates in the estimated 20-yr return value of daily maximum and minimum screen temperature is displayed in Fig. 11. It is apparent that there are substantial differences, both in the pattern and magnitude of change. The global mean change for $T_{max,20}$ is 3.14°C, whereas that for $T_{min,20}$ is 5.0°C.

The changes in $T_{min,20}$ and $T_{max,20}$ apparently occur for a variety of reasons. Over the tropical and temperate oceans the increases are roughly equal to the change that is observed in the mean screen temperature. This

suggests that the screen temperature distribution in these regions moves with the mean without change of shape. Apparently the ability of the ocean to moderate screen temperature variations in tropical and temperate regions is not strongly affected by the change in sea surface temperature, which occurs between the $1\times CO_2$ and $2\times CO_2$ climates.

Elsewhere (over landmasses and polar regions) there are changes in both the mean screen temperature and the shape of the screen temperature distribution. Increases in $T_{max,20}$ over continents (except Antarctica) are of the order of 5°C and range up to 10°C. The larger values occur in regions of North and South America and Eurasia, which experience a substantial decrease in soil moisture under CO_2 doubling (Boer et al. 1992, their Fig. 15). Reduced soil moisture means that maximum surface temperatures are less likely to be moderated by evaporative cooling.

Increases in $T_{min,20}$ over North America and western Asia are larger than the corresponding increases in $T_{max,20}$. This presumably occurs because these areas experience significantly less snow cover under CO_2 doubling resulting in an increase in the amount of solar radiation, that is absorbed at the ground. Some of the absorbed solar radiation subsequently warms the air overlying the surface at night and raises daily minimum temperatures.

Increases in $T_{min,20}$ over Siberia (which remains snow covered in winter under CO_2 doubling) are roughly comparable to the increases in $T_{max,20}$. Changes in both quantities are also roughly comparable over Africa. The band of large increases in $T_{max,20}$ that is seen around the edge of Greenland occurs because Greenland experiences a loss of snow cover in the $2\times CO_2$ climate. A corresponding change is not seen in $T_{min,20}$. Only small increases in $T_{max,20}$ occur in polar regions that retain some sea ice while large increases are observed in $T_{min,20}$. Large increases (4°–6 °C or more) in $T_{max,20}$ occur in regions that were formerly ice covered. Even larger (more than 20°C) increases are observed in $T_{min,20}$.

To emphasize the asymmetric character of change in extreme values of T_{max} and T_{min}, we display the change in $T_{max,20}$ and $T_{min,20}$ *relative* to the corresponding change in the annual mean of T_{max} and T_{min} in Fig. 12. As noted above, the change in return values is roughly equal to the change in the mean for both variables over the oceans. This is also true almost everywhere over the continents for T_{max}. In high latitudes, the increase in annual extremes of T_{max} is smaller than the increase in the annual mean by a factor of 2. This occurs because the change in the annual extremes of T_{max} at high latitudes primarily reflects temperature changes in summer, which are much smaller than the corresponding changes in winter (see, e.g., Fig. 2). For T_{min}, high values of the ratio $\Delta T_{min,20}/\Delta T_{min}$ clearly identify the areas where the snow and sea-ice cover have retreated in the warmer world.

The bootstrap procedure used to estimate confidence intervals of the change in screen temperature return values, shows that the changes under CO_2 doubling are statistically significant at less than the 5% level over most of the globe. This is not surprising since a change in air temperature is the primary response to the increased amount of carbon dioxide in the atmosphere. The signal tends to be more statistically significant over the oceans where the near-surface temperature variability is strongly constrained by the thermal inertia of the ocean. The signal is statistically less significant over the continents because natural variability is much larger. Estimation errors of return values become larger as the return period increases. For example, the portion of the globe where the change is statistically significant at the 5% level decreases from 98% for 10-yr return values of T_{max} to 90% for 50-yr return values and from 88% to 75% for corresponding T_{min} return values.

b. Precipitation

We have seen that the 20-yr records available from the $1\times CO_2$ and $2\times CO_2$ simulations appear to be adequate for making inferences about the extremes of screen temperature. This is true for both the 20-yr return values that have been discussed and for longer period (e.g., 50-yr) return values. That the inferences are reasonable is further corroborated by the fact that the estimated changes can be associated with other physical changes in the warmer climate.

Unfortunately, the same cannot be said for simulated daily precipitation or wind speed. Twenty-year return value estimates for daily precipitation made at grid points show a great deal of spatial noise and very little structure. This comes about for a number of reasons. Precipitation, even in the simulated climate, has a lot of small-scale spatial variability that masks the structure of the CO_2 doubling signal. Moreover, the signal itself is relatively weak; the mean daily precipitation, an indicator of the strength of the simulated hydrological cycle, increases by a modest 4% (see Table 1).

A rough estimate of the strength of the global signal in annual precipitation extremes may be obtained if we compare globally averaged changes in the estimated location parameter ξ in the GEV distribution with the globally averaged scale parameter α for different variables. The former is related to the absolute value of the signal and the latter characterizes variability. Table 2 shows the globally averaged estimates of location and scale parameters for the quantities considered in this study as well as the ratio of the globally averaged location parameter change under CO_2 doubling to the corresponding $1\times CO_2$ scale parameter. We see that the change of the location parameter normalized by the scale parameter is large for T_{max} and T_{min}, whereas the relative signal is very modest for daily precipitation and near-surface wind.

The change in the 20-yr return values of daily precipitation estimated for each grid box separately did not

$$\Delta T_{max,20}/\Delta T_{max}$$

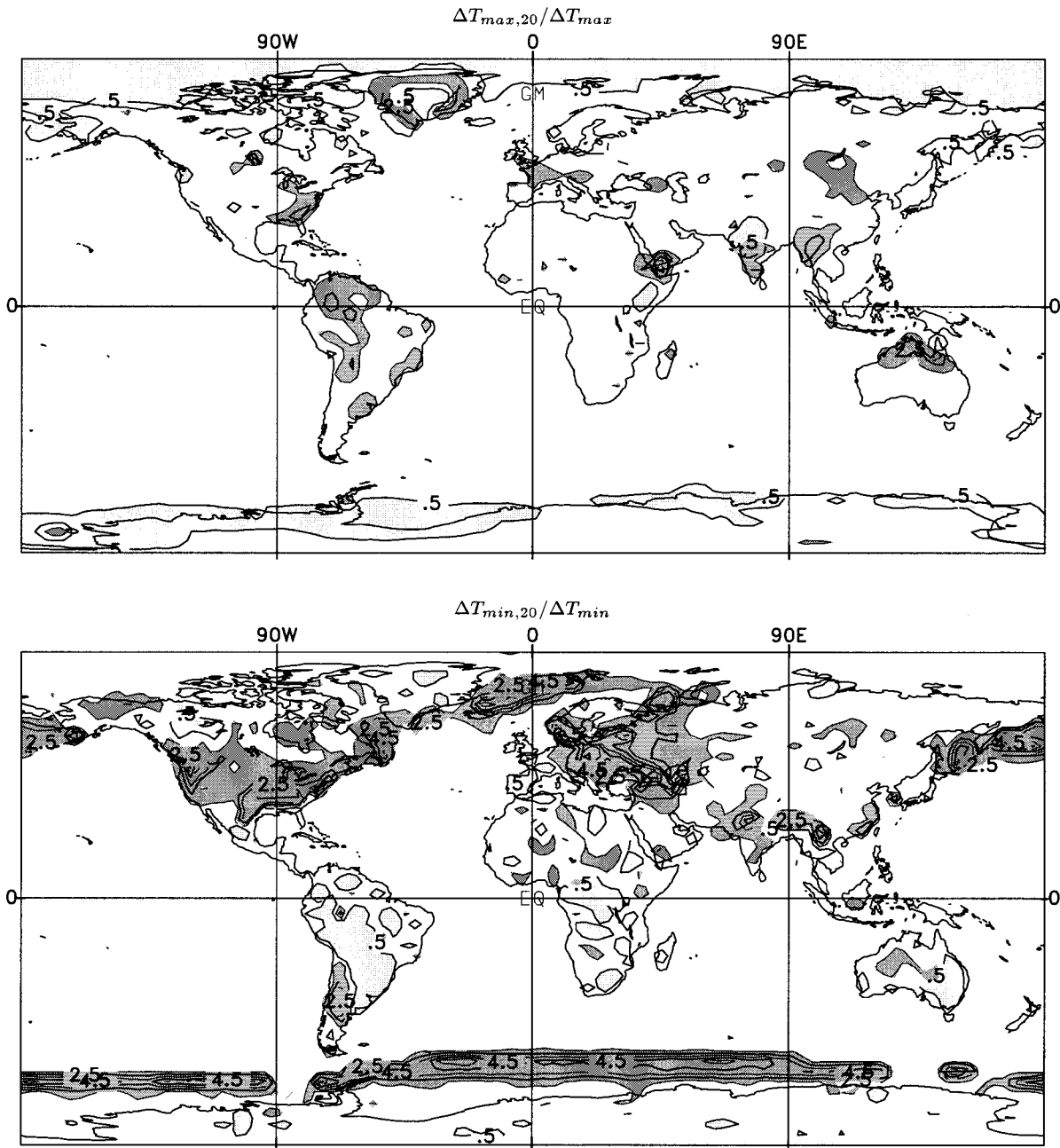$$\Delta T_{min,20}/\Delta T_{min}$$

FIG. 12. The estimated change in 20-yr return values for daily maximum (upper panel) and minimum (lower panel) screen temperature simulated by CCC GCM2 under CO_2 doubling divided by the corresponding change in annual mean maximum and minimum screen temperature. Contour interval 0.5. Light (dark) shading indicates regions with values below 0.5 (higher 1.5).

TABLE 2. Global means of the estimated location parameter ξ, scale parameter α in the GEV distribution in the simulated control (1 $\times$ CO_2) climate, and the ratio of the simulated change of the location parameter under CO_2 doubling to the scale parameter in the control run ($\Delta\xi/\alpha$) for T_{max} (°C), T_{min} (°C), P (mm day^{-1}), and S (m s^{-1}).

	T_{max} (°C)	T_{min} (°C)	P (mm day^{-1})	S (m s^{-1})
ξ	22.98	1.66	45.40	20.41
α	0.69	1.39	13.38	1.63
$\Delta\xi/\alpha$	4.52	3.40	0.30	0.50

appear to be significantly different from zero because the sampling errors in the quantile estimates from 20-yr time series are large. To reduce sampling errors, we applied a modified version of a multivariate technique described by Buishand (1991) in which extreme rainfall estimates are derived by combining data from several sites. The general idea is to assume that one or several parameters in the extreme value distribution are common for different sites. For example, Buishand (1991)
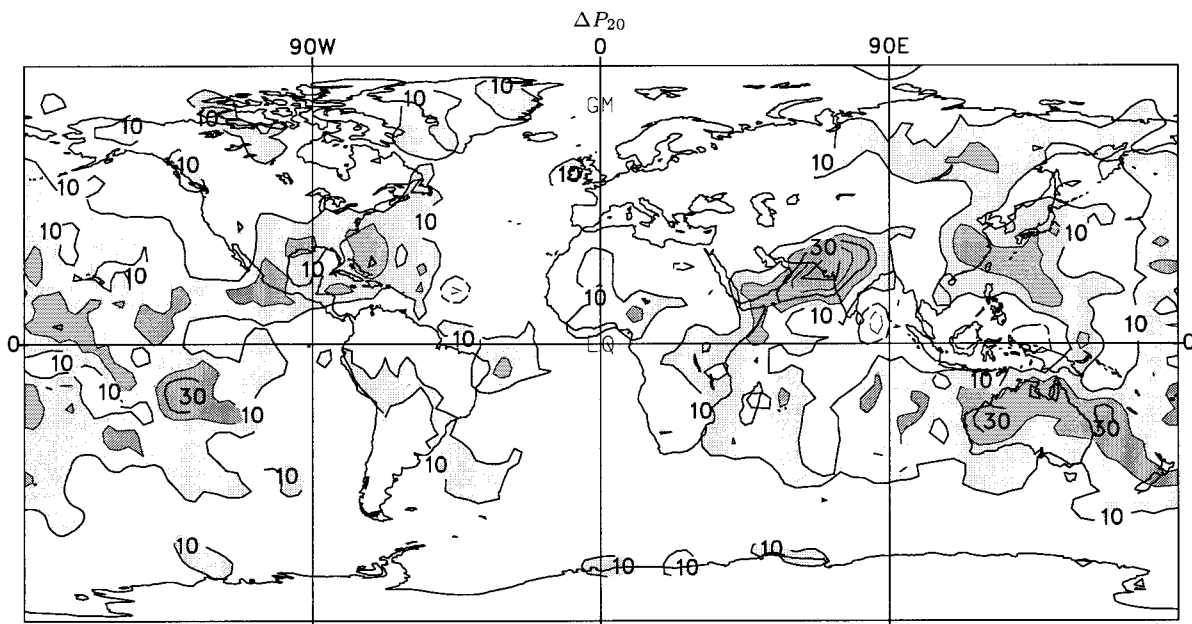
FIG. 13. The estimated change in smoothed 20-yr return values for daily accumulated precipitation simulated by CCC GCM2 under CO_2 doubling. Contour interval: 10 mm day^{-1}. Light (dark) shading indicates locations at which the 20-yr return value has increased by at least 10 (20) mm day^{-1}.

used the same shape parameter k for all sites and then estimated the location and scale parameters for each individual site by the maximum likelihood method. In our study we assume that the time series of annual maxima of daily precipitation in any four adjacent grid boxes (2 × 2), or any nine grid boxes (3 × 3) for even stronger smoothing, come from the same extreme value distribution. The "regional" L-moments estimates are obtained by averaging L moments estimated separately for each individual box over four, or nine, adjacent grid boxes. These regional L moments are then used to derive the regional parameters of the GEV distribution and the corresponding return value estimates.

Confidence intervals are constructed for the return value by assuming that the annual maxima of daily precipitation in the adjacent grid boxes are independent of each other. This assumption holds reasonably well in tropical and subtropical regions where the convective precipitation dominates the total rainfall. The average time period between the annual maxima occurring in the same year in any two adjacent grid boxes (not shown) exceeds at least 3 weeks in the Tropics and the subtropics where the large values of extreme daily precipitation are found in the model.

The change in the estimated 20-yr return values of the 3 × 3 smoothed extreme value distributions are displayed in Fig. 13. The change between $1 \times CO_2$ and $2 \times CO_2$ is positive almost everywhere on the globe. The strongest increase, over 50 mm day^{-1} (statistically significant at the 5% level), is found over the northwest of India where there is the intensification of the Asian summer monsoon under CO_2 doubling. Other parts of the

world with statistically significant increase in 20-yr return values of daily rainfall are northern Australia and to a lesser degree Central America and the Caribbean region as well as a small area south of Japan. A moderate decrease in return values is found over the tropical Indian Ocean and over the Malay Archipelago. The reduction of extreme precipitation in this area is not statistically significant.

Globally averaged, 20-yr return values increase 9 mm day^{-1} (11%) with respect to the control climate, which is greater than the 4% increase for the annual mean precipitation (Table 1). Over Canada, 20-yr return values increase approximately 7 mm day^{-1} (14%) on average.

Another way to express changes in frequency of extreme events is to define changes in return *periods*. In particular, we estimated the return periods of the 20-yr $1 \times CO_2$ return values in the $2 \times CO_2$ climate. The return periods of extreme daily precipitation (not shown) decrease substantially in the $2 \times CO_2$ run over broad areas where the daily extreme precipitation increases. For example, over North America, the return period of 20-yr return values is reduced by roughly a factor of 2, on average, indicating that extreme precipitation of that order occurs twice as often in the warmer world. Return periods are reduced by a factor of 5 over northwest India. In contrast, in dry areas, such as subtropical regions west of the African and North and South American continents as well as over northeast Africa, a modest decrease in 20-yr return values in the $2 \times CO_2$ integration leads to dramatically longer return periods.
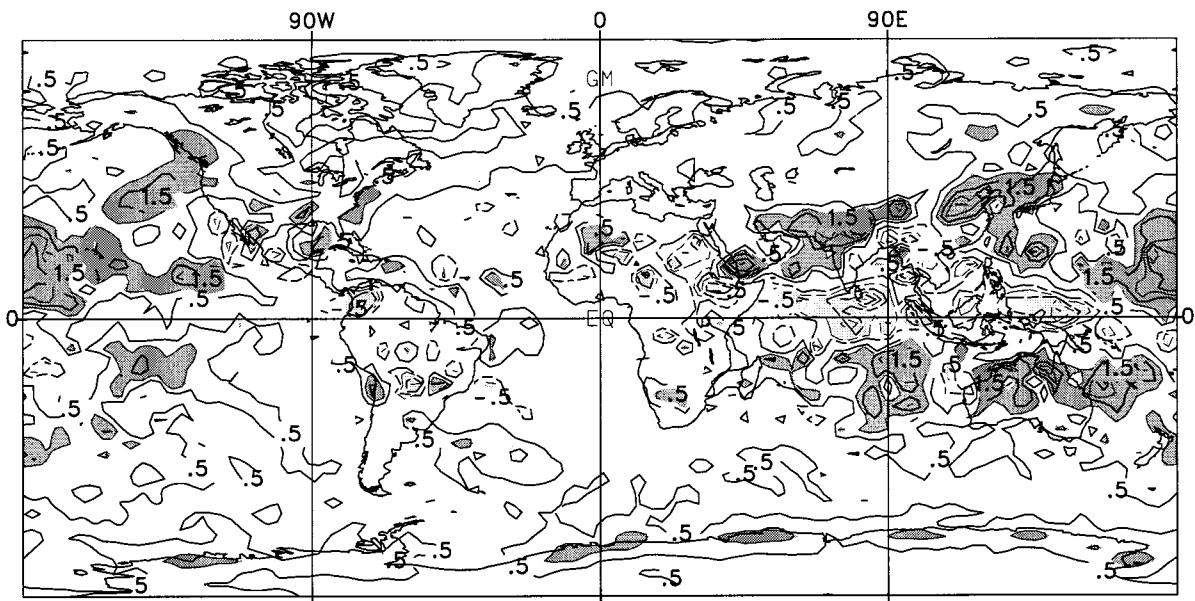
Simple univariate threshold methods can be used to

FIG. 14. Change in the amount of precipitation per rainday between the $1\times CO_2$ and $2\times CO_2$ climates. A rainday is defined as a day with 2 mm of precipitation or more. Contour interval: 0.5 mm day^{-1}. Dark (light) shading indicates regions in which the precipitation amount per rainday has increased (decreased) by at least 1 mm day^{-1}.

derive some other physically reasonable information about changes in the intensity and duration of precipitation. For example, Fig. 14 displays the change in the amount of precipitation that falls on a *rainday* where a rainday is defined as any day with 2 mm or more of precipitation. Decreases of 1 mm day^{-1} or more are seen primarily over the equatorial Indian Ocean and the equatorial western Pacific. Comparable increases in intensity are seen at subtropical latitudes over Asia, the central Pacific, the Indian Ocean, Australia, and the Pacific Northwest region of North America. Smaller increases in intensity are seen elsewhere. Similar maps computed using higher thresholds (e.g., 10 mm) reveal similar changes in the intensity of large precipitation events, but are contaminated by more small-scale noise than we see in Fig. 14.

Figure 15 displays the change in the number of raindays per year (again defined relative to the 2-mm threshold) in the warmer climate. High-latitude regions experience more frequent precipitation events. In midlatitudes the frequency of raindays is generally reduced, which is consistent with the reduction of baroclinic storm activity in the warmer world. The pattern of rainday frequency change in the Tropics and subtropics resembles closely that of mean precipitation change shown in Fig. 3.

Gordon et al. (1992) display similar figures derived from a simulation performed with the Commonwealth Scientific and Industrial Research Organisation (CSIRO) GCM that are in broad agreement with Figs. 14–15. The most notable differences are found in the Tropics and subtropics. In particular, the CSIRO GCM simulates a reduction in the number of raindays and in the

amount of rain per rainday under CO_2 doubling in the northern subtropical Pacific east of the date line, whereas the CCC GCM2 has the opposite tendency. Also, the intensification of the Asian summer monsoon is not as pronounced in the CSIRO model as in CCC GCM2.

c. Wind speed

The sampling variability that makes the changes in the extremes of precipitation difficult to interpret also affects the near-surface wind speed. According to Table 2 the strength of the globally averaged signal in the parameters of the GEV distribution for the near-surface wind are as small as that for precipitation. We applied the same smoothing technique to estimate return values of near-surface wind as for daily precipitation. However, the assumption of the independence of annual maxima of wind speed at adjacent grid points is no longer valid. The wind speed annual maxima are likely to occur on the same day in several adjacent grid points in broad areas over the globe. Thus, although the smoothing technique results in better organized patterns, it does not improve the signal-to-noise ratio to the extent that would be attained if the maxima were independent.

Figure 16 displays the change in the estimated 20-yr return value of 1000-mb wind speed under CO_2 doubling. Return values evidently increase in the Arctic and in a band surrounding Antarctica. That change is statistically significant at the 5% level and may be connected with sea-ice loss under CO_2 doubling. The atmosphere experiences less friction near the surface due to smaller surface roughness over open water areas in the warmer world. A modest increase of globally av-
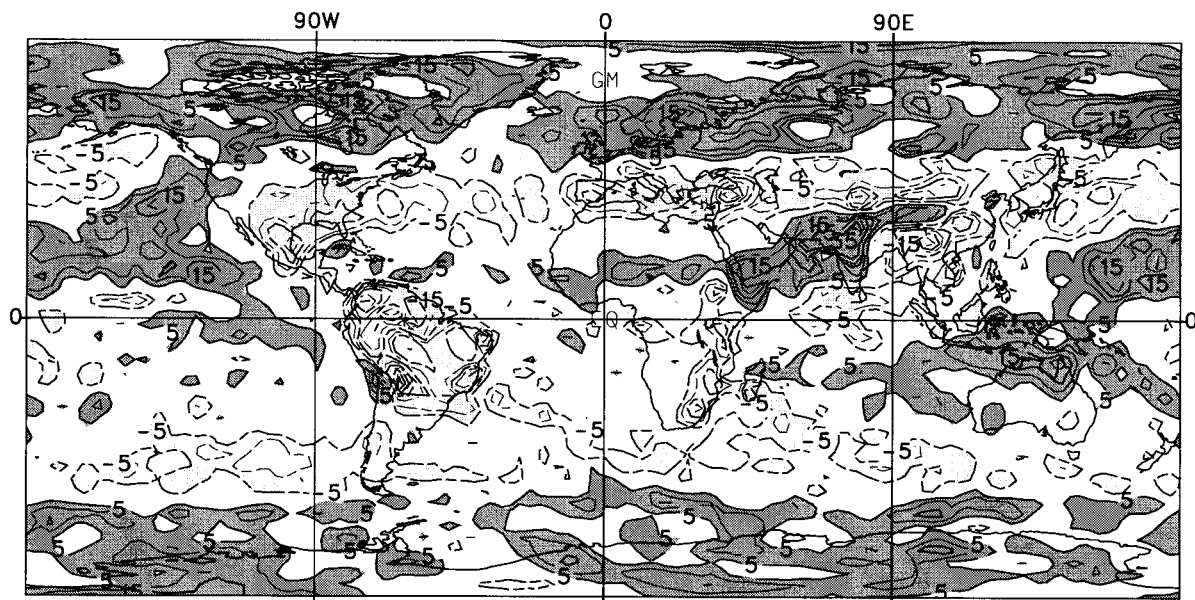
FIG. 15. Change in the number of raindays per year under CO_2 doubling. A rainday is defined as a day with 2 mm of precipitation or more. Contour interval: 5 days yr^{-1}. Dark (light) shading indicates regions in which the number of precipitation days per year has increased (decreased) by at least 5 days yr^{-1}.

eraged return values (see Table 1) is basically due to the extreme wind speed increase in the high latitudes.

In the midlatitudes and Tropics the changes in return values are marginal at best. There are some indications of the reduction in wind speed extremes over parts of the extratropics and in the tropical Indian Ocean. However, these changes are not statistically significant. The

only area, except the high latitudes, which apparently has a weakly significant increase in extreme wind speeds is northwest Europe. This increase is explained by a low pressure anomaly over northern Europe in the $2\times CO_2$ run (Boer et al. 1992, see their Fig. 30) which intensifies the zonal circulation over Europe and brings more storms into this area from the North Atlantic storm track.
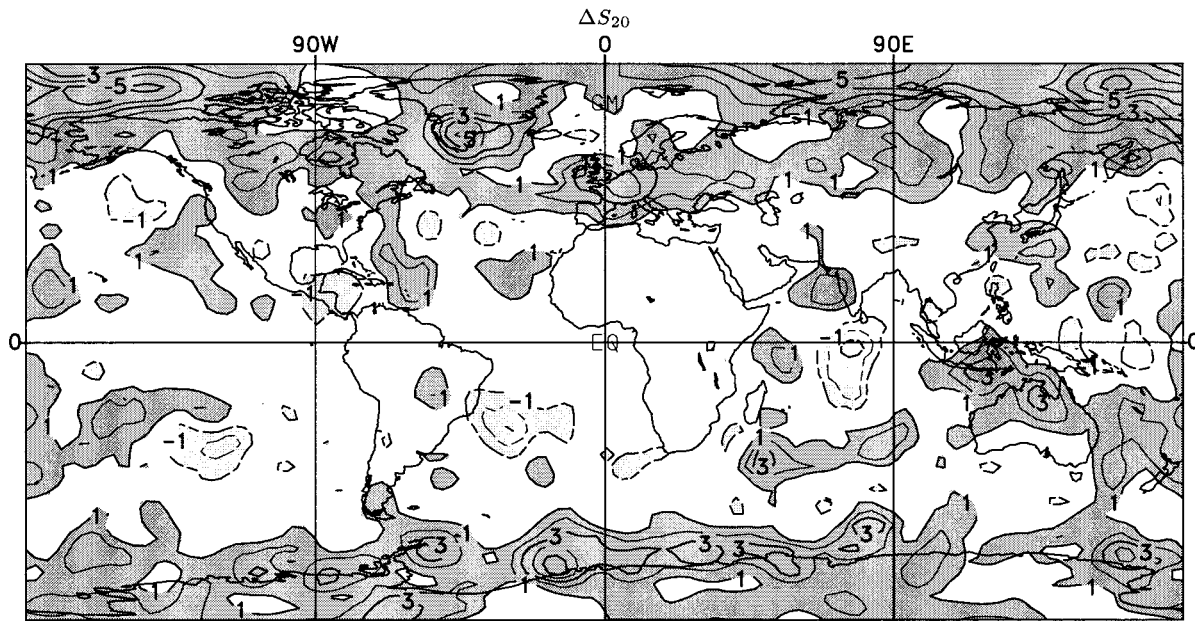

FIG. 16. The estimated change in smoothed 20-yr return values for 1000-mb wind speed simulated by CCC GCM2 under CO_2 doubling. Contour interval: 1 m s^{-1}. Dark (light) shading indicates regions in which the 20-yr return value has increased (decreased) by at least 1 m s^{-1}.
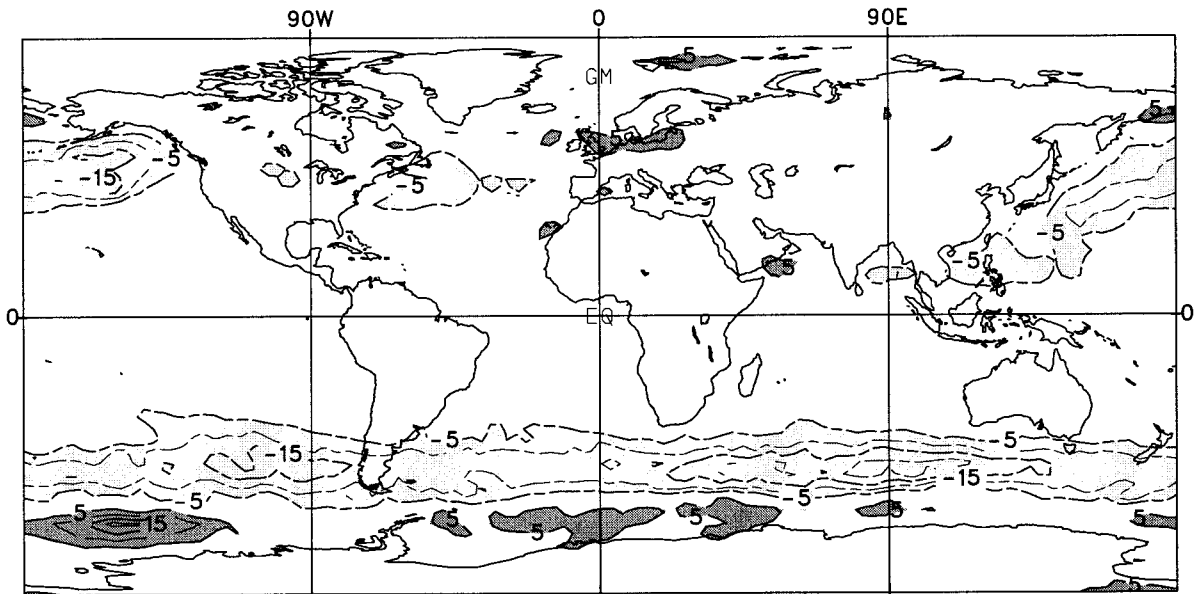
Fig. 17. Change in the number of strong wind days per year under CO_2 doubling, where a strong wind day is defined as a day with 1000-mb wind speed greater than 18 m s^{-1}.

More structure can be seen by estimating the change in frequency of threshold crossing for a moderately high threshold. Figure 17 illustrates the change in the number of days in which 1000-mb wind speed exceeds the 18 m s^{-1} threshold under CO_2 doubling. As in Fig. 16, we see some evidence for an increase in the number of moderately strong wind events in the areas where sea ice has retreated as well over northwest Europe, although not as pronounced as for extreme winds. The number of events in the storm tracks (the North Pacific, North Atlantic, and the southern roaring 40's) decreases. Note that the changes displayed in Fig. 17 are more similar in structure to the changes in the mean (Fig. 4) than those in Fig. 16. The time of occurrence of extreme events does not change substantially in the warmer world.

Beersma et al. (1997) obtained a similar result in a study of the change in frequency of extratropical storms in the North Atlantic region under CO_2 doubling as simulated by a high-resolution atmospheric model. They found a negative pressure anomaly over Scandinavia in the $2\times CO_2$ experiment. This was associated with a marginal decrease in the frequency of deep depressions and intensity of extreme winds in the central and northern North Atlantic and a modest increase of extreme winds in the North Sea and over central Europe. Lambert (1995) analyzed the cyclone frequency in a 5-yr record of the equilibrium simulations used in this study and found an increase of intense cyclones in the $2\times CO_2$ climate, especially in the Northern Hemisphere, whereas the total number of cyclones decreases significantly in the warmer world. In our study we did not find any statistically significant evidence of increased wind extremes in the middle latitudes, except perhaps over

northwest Europe. Also König et al. (1993) found a reduction in Northern Hemisphere cyclone frequency in some regions and a shift of the cyclone tracks in other regions, but no sign of significant increase of cyclone frequency.

6. Summary

An extreme value analysis of the climate simulated by CCC GCM2 is discussed. Two kinds of techniques were applied to the data. First, the annual daily maxima of several near-surface variables were fitted to the Generalized Extreme Value distribution at every grid point by the method of L moments. Ten-, 20- and 50-yr return values were estimated from the fitted distribution. Second, a threshold crossing technique was used to examine the frequency occurrence of moderately large events at each grid point. The results for the control $1\times CO_2$ simulation were compared with those obtained from the NCEP–NCAR reanalysis data and from Canadian station data.

Changes in extremes under CO_2 doubling are identified. A simple smoothing technique was used to analyze the changes in return values of daily precipitation and 1000-mb wind speed in the warmer CO_2 world because the signal in these quantities is small. The technique assumes that the time series of annual extremes in the adjacent grid boxes come from approximately the same statistical distribution.

In summary:

- The extremes of the control climate are reasonably close to those of the observed climate.
- Changes in the extremes of daily minimum and max-

imum screen temperature can be reasonably well estimated with the available 20-yr simulations, and connections to other physical changes in the warmer world can be speculated upon.

- The patterns of the change in annual extremes of T_{max} and T_{min} are different. Because annual extremes of T_{max} and T_{min} usually occur in opposite seasons in the extratropics, the physical processes that cause change in the warmer world are different. Changes in the return values of T_{min} are substantially larger than those in the annual mean of T_{min} in areas where snow and sea ice have retreated.

- Changes in the extremes of precipitation and near-surface wind speed are more difficult to analyze since the CO_2 signal in these variables is much weaker. Nonetheless, changes can be identified if a ''peaks-over-threshold'' method is applied.

- The extreme wind speed is generally reduced in the middle latitudes, which is probably related to the reduced meridional temperature gradient and weaker baroclinic activity in the warmer world. The enhancement of wind extremes in high latitudes is connected to reduced surface roughness due to sea-ice retreat. There are some indications of increased wind speed extremes over Europe in the simulated warmer world, which is related to the negative pressure anomaly over northern Europe and Scandinavia in the $2 \times CO_2$ simulations.

- The precipitation extremes increased almost everywhere over the globe. The relative change in globally averaged extreme precipitation is larger than that in mean precipitation. This result is in general agreement with findings of other studies (e.g., Cubasch et al. 1995). Globally averaged, the 20-yr return values increase by about 1 cm day^{-1}, or more than 10%. Assuming that this additional rainfall amount can fall in a much smaller area than the model grid box, for example, in a squall line, one can imagine much larger increases of local rainfall.

- Return periods of extreme precipitation are shortened by a factor 2 and more in the $2 \times CO_2$ climate in many parts of the world. This is consistent with many other model studies that also report shorter return periods for intense precipitation events (e.g., McGuffie et al. 1998, manuscript submitted to *Int. J. Climatol.*). The number of raindays per year generally increases in polar regions and decreases in midlatitudes. A similar result was found by Gordon et al. (1992). Also Cubasch et al. (1995) found that the average waiting time between precipitation events increases significantly in the middle latitudes, but it decreases in high latitudes and in the Tropics under CO_2 doubling and tripling.

As a final note, we must emphasize that the present study describes changes under CO_2 doubling in an *equilibrium* simulation. The details of some of the findings and arguments made in this paper may therefore not extend to more realistic transient experiments with a coupled atmosphere–ocean GCM. The analysis of changes in the extremes in an ensemble of transient simulations with a coupled GCM performed at the CCCma is currently under way.

REFERENCES

Beersma, J. J., K. M. Rider, G. J. Komen, E. Kaas, and V. V. Kharin, 1997: An analysis of extra-tropical storms in the North Atlantic region as simulated in a control and $2 \times CO_2$ time-slice experiment with a high resolution atmospheric model. *Tellus,* **49A,** 347–361.

Bengtsson, L., M. Botzet, and M. Esch, 1995: Hurricane-type vortices in a general circulation model. *Tellus,* **47A,** 175–196.

——, ——, and ——, 1996: Will greenhouse gas-induced warming over the next 50 years lead to higher frequency and greater intensity of hurricanes? *Tellus,* **48A,** 57–73.

Boer, G. J., 1993: Climate change and the regulation of the surface moisture and energy balance. *Climate Dyn.,* **8,** 225–239.

——, 1995: Some dynamical consequences of greenhouse gas warming. *Atmos.–Ocean,* **33,** 731–751.

——, N. A. McFarlane, and M. Lazare, 1992: Greenhouse gas-induced climate change simulated with the CCC Second-Generation General Circulation Model. *J. Climate,* **5,** 1045–1077.

Bromwich, D. H., and R.-Y. Tzeng, 1994: Simulation of the modern Arctic climate by NCAR CCM1. *J. Climate,* **7,** 1050–1069.

Buishand, T. A., 1989: Statistical extremes in climatology. *Statist. Neerland.,* **43,** 1–30.

——, 1991: Extreme rainfall estimation by combining data from several sites. *Hydrol. Sci. J.,* **36,** 345–365.

Cao, H. X., J. F. V. Mitchell, and J. R. Lavery, 1992: Simulating diurnal range and variability of surface temperature in a global climate model for present and doubled CO_2 climates. *J. Climate,* **5,** 920–943.

Carnell, R. E., C. A. Senior, and J. F. B. Mitchell, 1996: An assessment of measures of storminess: Simulated changes in Northern Hemisphere winter due to increasing CO_2. *Climate Dyn.,* **12,** 467–476.

Cubasch, U., K. Hasselmann, H. Hock, E. Maier-Reimer, U. Mikolajewicz, B. D. Santer, and R. Sausen, 1992: Time-dependent greenhouse warming computations with a coupled ocean–atmosphere model. *Climate Dyn.,* **8,** 55–69.

——, J. Waszkewitz, G. Hegerl, and J. Perlwitz, 1995: Regional climate changes as simulated in time-slice experiments. *Climate Change,* **31,** 273–304.

Davis, R. A., 1982: The rate of convergence in distribution of the maxima. *Statist. Neerland.,* **36,** 31–35.

Efron, B., 1982: *The Jackknife, the Bootstrap and Other Resampling Plans.* SIAM, 92 pp.

Farago, T., and R. W. Katz, 1990: Extremes and design values in climatology. WMO/TD-386, 43 pp.

Fisher, R. A., and L. H. C. Tippett, 1928: Limiting forms of the frequency distribution of the largest or smallest members of a sample. *Proc. Cambridge Philos. Soc.,* **24,** 180–190.

Gnedenko, B., 1943: Sur la distribution limite du terme maximum d'une série aléatoire. *Ann. Math.,* **44,** 423–453.

Gordon, H. B., P. H. Whetton, A. B. Pittock, A. M. Fowler, and M.

R. Haylock, 1992: Simulated changes in daily rainfall intensity due to the enhanced greenhouse effect: Implications for extreme rainfall events. *Climate Dyn.,* **8,** 83–102.

Gumbel, E. J., 1958: *Statistics of Extremes.* Columbia University Press, 375 pp.

Hall, N. M. J., B. J. Hoskins, P. J. Valdes, and C. A. Senior, 1994: Storm tracks in a high resolution GCM with doubled CO_2. *Quart. J. Roy. Meteor. Soc.,* **120,** 1209–1230.

Hennessy, K. J., and A. B. Pittock, 1995: Greenhouse warming and threshold temperature events in Victoria, Australia. *Int. J. Climatol.,* **15,** 591–612.

Hogg, W. D., and D. A. Carr, 1985: *Rainfall Frequency Atlas for Canada.* Canadian Government Publishing Centre, 89 pp.

Hosking, J. R. M., 1990: L-moments: Analysis and estimation of distributions using linear combinations of order statistics. *J. Roy. Stat. Soc.,* **52B,** 105–124.

——, 1992: Moments or L-moments? An example comparing the two measures of distributional shape. *Amer. Stat.,* **46,** 186–189.

——, J. R. Wallis, and E. F. Wood, 1985: Estimation of the generalized extreme-value distribution by the method of probability-weighted moments. *Technometrics,* **27,** 251–261.

Houghton, J. T., G. J. Jenkins, and J. J. Ephraums, Eds., 1990: *Climate Change: The IPCC Scientific Assessment.* Cambridge University Press, 365 pp.

——, L. G. Meira-Filho, B. A. Callander, N. Harris, A. Kattenberg, and K. Maskell, Eds., 1996: *Climate Change 1995: The Science of Climate Change.* Cambridge University Press, 572 pp.

Huang, J.-P, and G. R. North, 1996: Cyclic spectral analysis fluctuations in a GCM simulation. *J. Atmos. Sci.,* **53,** 370–379.

Kalnay, E., and Coauthors, 1996: The NCEP/NCAR 40-Year Reanalysis project. *Bull. Amer. Meteor. Soc.,* **77,** 437–471.

König, W., R. Sausen, and F. Sielmann, 1993: Objective verification of cyclones in GCM simulations. *J. Climate,* **6,** 2217–2231.

Lambert, S. J., 1995: The effect of enhanced greenhouse warming on winter cyclone frequencies and strengths. *J. Climate,* **8,** 1447–1452.

——, J. Sheng, and J. S. Boyle, 1995: Cyclone frequencies and intraseasonal variability in GCMs. *Proc. First Int. AMIP Scientific Conf.,* Monterey, CA, WMO/TD-72, 199–204.

Leadbetter, M. R., G. Lindgren, and H. Rootzén, 1983: *Extremes and Related Properties of Random Sequences and Processes.* Springer-Verlag, 336 pp.

McFarlane, N. A., G. J. Boer, J.-P. Blanchet, and M. Lazare, 1992: The Canadian Climate Centre Second Generation General Circulation Model and its equilibrium climate. *J. Climate,* **5,** 1013–1044.

Mearns, L. O., 1993: Implications of global warming for climate variability and the occurrence of extreme climate events. *Drought Assessment, Management and Planning: Theory and Case Studies,* D. A. Wilhite, Ed., Kluwer, 109–130.

——, S. H. Schneider, S. L. Thompson, and L. R. McDaniel, 1990: Analysis of climate variability in general circulation models: Comparison with observations and changes in variability with $2\times CO_2$. *J. Geophys. Res.,* **95** (D12), 20 469–20 490.

Murphy, J. M., 1995: Transient response of the Hadley Centre model to increasing carbon dioxide. Part I: Control climate and flux correction. *J. Climate,* **8,** 36–56.

NCEP–NCAR, cited 1997a: Notes concerning reanalysis: Problem with skin temperature. [Available online from ftp://wesley. wwb.noaa.gov/pub/reanal/random_notes/problem.tmp.Z.]

——, cited 1997b: Notes concerning reanalysis: Precipitation. [Available online from ftp://wesley.wwb.noaa.gov/pub/reanal/random_notes/precip.Z.]

Noda, A., and T. Tokioka, 1989: The effect of doubling the CO_2 concentration on convective and non-convective precipitation in a general circulation model coupled with a simple mixed layer ocean model. *J. Meteor. Soc. Japan,* **67,** 1057–1069.

Osborn, T. J., and M. Hulme, 1997: Development of a relationship between station and grid-box rainday frequencies for climate model evaluation. *J. Climate,* **10,** 1885–1908.

Parey, S., 1994: Simulations de trente ans $1\times CO_2$, $2\times CO_2$, $3\times CO_2$ avec le modele du LMD ($64 \times 50 \times 11$) premiers resultats. EDF, Directions des Etudes et Recherches, HE-33/94/008, 103 pp. [Available from Electricté de France, Groupe Météorologie et Climat, 6, Quai Watier, Boite Postale 49, F-78401 Chatou Cedex, France.]

Revfeim, K. J. A., and W. D. Hessel, 1984: More realistic distributions for extreme wind gusts. *Quart. J. Roy. Meteor. Soc.,* **110,** 505–514.

Rind, D. R., R. Goldberg, and R. Ruedy, 1989: Change in climate variability in the 21st century. *Climate Change,* **14,** 5–37.

Senior, C. A., 1995: The dependence of climate sensitivity on the horizontal resolution of a GCM. *J. Climate,* **8,** 2860–2880.

Skelly, W. C., and A. Henderson-Sellers, 1996: Grid-box or grid-point: What type of precipitation data do GCMs deliver? *Int. J. Climatol.,* **16,** 1079–1086.

Smith, R. L., 1989: Extreme value analysis of environmental time series: An application to trend detection in ground-level ozone. *Stat. Sci.,* **4,** 367–393.

Tabony, R. C., 1983: Extreme value analysis in meteorology. *Meteor. Mag.,* **112,** 77–98.

Tiago de Oliveira, J., 1986: Extreme values and meteorology. *Theor. Appl. Climatol.,* **37,** 184–193.

Windelband, M., and R. Sausen, 1993: Some extreme value statistics of a global warming simulation. Meteor. Inst. der Univ. Hamburg Rep. 12, 50 pp. [Available from Meteor. Inst. der Univ. Hamburg, Bundesstrasse 55, Hamburg D-20146, Germany.]

Zwiers, F. W., and W. H. Ross, 1991: An alternative approach to the extreme value analysis of rainfall data. *Atmos.–Ocean,* **29,** 437–461.